Modeling viscoelastic behavior of arterial walls and their interaction with pulsatile blood flow — Source link ⌴

Sunčica Čanić, Josip Tambača, Giovanna Guidoboni, Andro Mikelić ...+2 more authors

Related papers:

- On the coupling of 3D and 1D Navier-Stokes equations for flow problems in compliant vessels

- Blood Flow in Compliant Arteries: An Effective Viscoelastic Reduced Model, Numerics, and Experimental Validation

- Computational vascular fluid dynamics: problems, models and methods

- Fluid-structure interaction in blood flow capturing non-zero longitudinal structure displacement

- Arterial Wall Mechanics in Conscious Dogs Assessment of Viscous, Inertial, and Elastic Moduli to Characterize Aortic Wall Behavior

MODELING VISCOELASTIC BEHAVIOR OF ARTERIAL WALLS AND THEIR INTERACTION WITH PULSATILE BLOOD FLOW[*]

SUNČICA ČANIĆ[†], JOSIP TAMBAČA[‡], GIOVANNA GUIDOBONI[†], ANDRO MIKELIĆ[§], CRAIG J. HARTLEY[¶], AND DOREEN ROSENSTRAUCH[‖]

Abstract. Fluid-structure interaction describing wave propagation in arteries driven by the pulsatile blood flow is a complex problem. Whenever possible, simplified models are called for. One-dimensional models are typically used in arterial sections that can be approximated by the cylindrical geometry allowing axially symmetric flows. Although a good first approximation to the underlying problem, the one-dimensional model suffers from several drawbacks: the model is not closed (an ad hoc velocity profile needs to be prescribed to obtain a closed system) and the model equations are quasi-linear hyperbolic (oversimplifying the viscous fluid dissipation), typically producing shock wave solutions not observed in healthy humans. In this manuscript we derived a simple, *closed* reduced model that accounts for the viscous fluid dissipation to the leading order. The resulting fluid-structure interaction system is of hyperbolic-parabolic type. Arterial walls were modeled by a novel, linearly *viscoelastic* cylindrical Koiter shell model and the flow of blood by the incompressible, viscous Navier–Stokes equations. Kelvin–Voigt-type viscoelasticity was used to capture the hysteresis behavior observed in the measurements of the arterial stress-strain response. Using the a priori estimates obtained from an energy inequality, together with the asymptotic analysis and ideas from homogenization theory for porous media flows, we derived an effective model which is an ϵ^2-approximation to the three-dimensional axially symmetric problem, where ϵ is the aspect ratio of the cylindrical arterial section. Our model shows two interesting features of the underlying problem: bending rigidity, often times neglected in the arterial wall models, plays a nonnegligible role in the ϵ^2-approximation of the original problem, and the viscous fluid dissipation imparts long-term viscoelastic memory effects on the motion of the arterial walls. This does not, to the leading order, influence the hysteresis behavior of arterial walls. The resulting model, although two-dimensional, is in the form that allows the use of one-dimensional finite element method techniques producing fast numerical solutions. We devised a version of the Douglas–Rachford time-splitting algorithm to solve the underlying hyperbolic-parabolic problem. The results of the numerical simulations were compared with the experimental flow measurements performed at the Texas Heart Institute, and with the data corresponding to the hysteresis of the human femoral artery and the canine abdominal aorta. Excellent agreement was observed.

[†]Department of Mathematics, University of Houston, 4800 Calhoun Rd., Houston, TX 77204-3476 (canic@math.uh.edu, gio@math.uh.edu). The first author's research was supported by the NSF under grants DMS0245513 and DMS-0337355, and by the NSF and NIH under grant DMS-0443826.

[‡]Department of Mathematics, University of Zagreb, Bijenička 30, 10000 Zagreb, Croatia (tambaca@math.hr). This author's research was supported by the NSF and NIH under grant DMS-0443826.

[§]Institue Camille Jordan, UFR Mathématiques, Site de Gerland, Université Claude Bernard Lyon 1, Bat. A, 50 avenue Tony Garnier, 69367 Lyon Cedex 07, France (mikelic@univ-lyon1.fr). This author's research was supported by the NSF and NIH under grant DMS-0443826.

[¶]Department of Medicine, Section of Cardiovascular Sciences, Baylor College of Medicine, Houston, TX 77030 (chartley@bcm.edu). This author's research was supported by the NSF and NIH under grant DMS-0443826, and by the NIH under grant HL22512.

[‖]Texas Heart Institute at St. Luke's Episcopal Hospital, Houston, TX 77030, and the University of Texas Health Science Center at Houston, Houston, TX 77030 (doreen.rosenstrauch@uth.tmc.edu). This author's research was supported by the NSF and NIH under grant DMS-0443826, and by the Roderick Duncan McDonald Foundation at St. Luke's Episcopal Hospital.

1. Introduction. The study of flow of a viscous incompressible fluid through a compliant tube is of interest to many applications. A major application is blood flow through human arteries. Understanding wave propagation in arterial walls, local hemodynamics, and temporal wall shear stress gradient is important in understanding the mechanisms leading to various complications in the cardiovascular function. Many clinical treatments can be studied in detail only if a reliable model describing the response of arterial walls to the pulsatile blood flow is considered.

It has been well accepted that in medium-to-large arteries blood can be modeled as a viscous, incompressible Newtonian fluid. Although blood is a suspension of red blood cells, white blood cells, and platelets in plasma, its non-Newtonian nature due to the particular rheology is relevant in small arteries (arterioles) and capillaries where the diameter of the arteries becomes comparable to the size of the cells. In medium-to-large arteries, such as the coronary arteries (medium) and the abdominal aorta (large), the Navier–Stokes equations for an incompressible viscous fluid are considered to be a good model for blood flow.

Devising an accurate model for the mechanical behavior of arterial walls is more complicated. Arterial walls are anisotropic and heterogeneous, composed of layers with different biomechanical characteristics [21, 22, 29, 44]. A variety of different models has been suggested in the literature to model the mechanical behavior of arteries [1, 2, 3, 21, 22, 23, 29, 27, 33, 44, 51]. They range from the detailed description of each of the layers to the average description of the total mechanical response of the vessel wall assuming homogeneous, linearly elastic behavior.

To study the *coupling* between the motion of the vessel wall and pulsatile blood flow, a detailed description of the vessel wall biomechanical properties may lead to a mathematical and numerical problem whose complexity is beyond today's computational capabilities. The nonlinearity of the underlying fluid-structure interaction is so severe that even simplified description of the vessel wall mechanics assuming homogeneous, linearly elastic behavior leads to the complicated numerical algorithms with challenging stability and convergence properties. To devise a mathematical model that will lead to a problem which is amenable to numerical methods producing computational solutions in a reasonable time-frame, various simplifications need to be introduced. They can be based on the simplifying model *assumptions* capturing only the most important physics of the problem and/or on the simplifications utilizing *special problem features* such as, for example, special geometry, symmetry, and periodicity.

A common set of simplifying assumptions that captures only the most important physics in the description of the mechanical properties of arterial walls includes homogeneity of the material with "small" displacements and "small" deformation gradients leading to the hypothesis of linear elasticity. A common set of special problem features that leads to simplifying models includes "small" vessel wall thickness allowing a reduction from three-dimensional models to two-dimensional shell models, and cylindrical geometry of a section of an artery where no branching is present allowing the use of cylindrical shell models. Neglecting bending rigidity of arteries, studied in [18, 21], reduces the shell model to a membrane model. Further simplifications include axial symmetry of the loading exerted by the blood flow to the vessel walls in the approximately straight cylindrical sections, leading to axially symmetric models with a potential of further reduction to one-dimensional models. One-dimensional models, although a good first approximation to the underlying problem, suffer from several drawbacks: they are not closed (an ad hoc velocity profile needs to be prescribed to

obtain a closed system), and the model equations are quasi-linear hyperbolic, typically producing shock wave solutions, not observed in healthy humans [5]. In particular, the wall shear stress calculated using one-dimensional models is a consequence of the form of the prescribed velocity profile.

Two-dimensional and three-dimensional models of the fluid-structure interaction between the incompressible viscous fluid flow and the motion of a linearly elastic cylindrical membrane are rather complex. Often times additional ad hoc terms of viscoelastic nature are added to the vessel wall model to provide stability and convergence of the underlying numerical algorithm [40, 44], or to provide enough regularity in the proof of the existence of a solution [10, 16, 24, 49], thereby showing well-posedness of the underlying problem. To this day there is no analytical result proving well-posedness of the fluid-structure interaction problem without assuming that the structure model includes the higher-order derivative terms capturing some kind of viscoelastic behavior [10, 16, 24, 49], or with the terms describing bending (flexion) rigidity in elastic shells or plates [10, 15]. In fact, current literature on well-posedness of the fluid-structure interaction between a viscous incompressible Newtonian fluid and a viscoelastic structure includes many additional simplifying assumptions such as the smallness of the data [49], periodic boundary conditions [24, 49], or flow in a closed cavity [10, 15, 16], not appropriate for the blood-flow application. Thus, the well-posedness of the fluid-structure interaction problem describing blood flow in compliant (elastic or viscoelastic) arteries remains an open problem. However, even in those simplifying problems when the data is infinitesimally small the higher-order regularizing terms in the structure model play a crucial role in providing the stabilizing mechanism. Thus, ignoring the terms that account for bending rigidity of the vessel walls and/or viscous dissipation might mean oversimplifying the physics, giving rise to a problem which might not have a solution.

Keeping this in mind we turn to the theory of elastic/viscoelastic shells to model the mechanical properties of arterial walls. Thus, we will be assuming that the vessel walls are homogeneous, that the thickness of the wall is small in comparison to the vessel radius, and that the state of stress is approximately plane, allowing us to consider shell theory. See section 2. The equations of shell theory have been derived by many authors; see [19] and the references therein. Due to variations in approach and rigor the variety of equations occurring in the literature is overwhelming. Among all the equations of shell theory the Koiter shell equations appear to be the simplest consistent first approximation in the general theory of thin elastic shells [32, 31]. In addition, they have been mathematically justified using asymptotic methods to be consistent with three-dimensional elasticity [12, 13]. Ciarlet and Lods showed in [12] that the Koiter shell model has the same asymptotic behavior as the three-dimensional membrane model, the bending model, and the generalized membrane model in the respective regimes in which each of them holds. Motivated by these remarkable properties of the Koiter shell model, in this manuscript we derived the Koiter shell equations for the cylindrical geometry and extended the linearly elastic Koiter model to include the viscous effects observed in the measurements of the mechanical properties of vessel walls [1, 2, 3]. We utilized the Kelvin–Voigt viscoelastic model, which has been shown in [1, 2, 3] to approximate well the experimentally measured viscoelastic properties of the canine aorta and of the human femoral and carotid arteries. In [43] a version of the Kelvin–Voigt model was used to model the vessel walls as a linearly viscoelastic membrane. In the Kelvin–Voigt model the total stress is linearly proportional to the strain and the time-derivative of strain. More

precisely, for a three-dimensional isotropic and homogeneous body, the Kelvin–Voigt model relates the total stress tensor, whose components we denote by t_{kl}, to the infinitesimal strains e_{kl} and the time-derivative of the strains $\partial_t e_{kl}$ through the following relationship [20]:

$$(1.1) \qquad t_{kl} = (\lambda_e + \lambda_v \partial_t) I_e \delta_{kl} + 2(\mu_e + \mu_v \partial_t) e_{kl}, \quad k, l = 1, 2, 3,$$

where λ_e and μ_e are the Lamé constants of elasticity, λ_v and μ_v are their corresponding viscoelastic counterparts, δ_{kl} is the Kronecker delta, and $I_e := \sum_{i=1}^{3} e_{ii}$. In section 8 we show that the fluid-structure interaction algorithm based on the viscoelastic Koiter shell equations coupled with the Navier–Stokes equations for a viscous incompressible fluid captures the experimentally measured viscoelastic properties of arterial walls in the human femoral artery and in the canine aorta. This is, in a nutshell, the main result of this manuscript; using the a priori estimates based on an energy inequality, coupled with the asymptotic analysis and homogenization theory, we derived an effective, closed fluid-structure interaction model and a fast numerical solver whose solutions capture the viscoelastic properties of major arteries. We show that our effective model approximates the original three-dimensional axially symmetric problem to the ϵ^2-accuracy, where ϵ is the aspect ratio of the cylindrical domain (vessel). Our reduced, effective model reveals several interesting features of the coupled fluid-structure interaction problem:

(1) Our model explicitly shows how the leading-order viscous fluid dissipation imparts long-term viscoelastic memory effects on the motion of the vessel wall. This is studied in section 5; see (5.11). We show that this does not influence, to the leading order, the viscoelastic hysteresis loop observed in the stress-strain (or the pressure-diameter) measurements of the arterial viscoelastic properties.

(2) Our model shows that bending rigidity of vessel walls plays a nonnegligible role in the asymptotic behavior of the underlying fluid-structure interaction problem. See the equation for p^0 in (4.17). We found that for the parameters describing blood flow through medium-to-large arteries the leading-order terms in the coupling of the stresses at the vessel wall include not only the membrane terms but also a correction accounting for the bending rigidity of the wall, often times neglected in the description of the mechanical properties of vessel walls.

We developed a fast numerical solver based on the one-dimensional finite element approach and compared the computational solution with the experimental measurements. First, the reduced *elastic* model was tested experimentally using a mock circulatory flow loop with latex tubing, assembled at the Research Laboratory at the Texas Heart Institute. Then the *viscoelastic* model was compared to the hysteresis measurements of the viscoelastic properties of the human femoral artery and the canine aorta. In both cases, excellent agreement between the experiment and the numerical solution was obtained.

2. The viscoelastic cylindrical Koiter shell model. In this section we focus on the derivation of the viscoelastic cylindrical Koiter shell model. We begin with the linearly elastic Koiter shell model as it was derived in [31, 32] and specialize it to the cylindrical shell geometry. Following standard texts in conventional plate and shell theories (see, for example, [20, 41, 45, 50, 52]), we then derive the stress-strain relationship for the Koiter shell model and extend it to include the Kelvin–Voigt viscoelasticity, which has been experimentally observed to approximate well the viscoelastic mechanical properties of arterial walls [1, 2, 3]. We summarize the main steps next.

2.1. The linearly elastic Koiter shell model. Consider a clamped cylindrical shell with the reference radius of the middle surface equal to $r = R$, with the shell thickness h and the cylinder length L, $z \in (0, L)$. The basic assumptions under which the Koiter shell model holds are [31, 32] that

- the shell is thin ($h/R \ll 1$);
- the strains are small everywhere, although large deflections are admitted, and the strain energy per unit volume of the undeformed body is represented by the quadratic function of the strain components for an isotropic solid (Hooke's law);
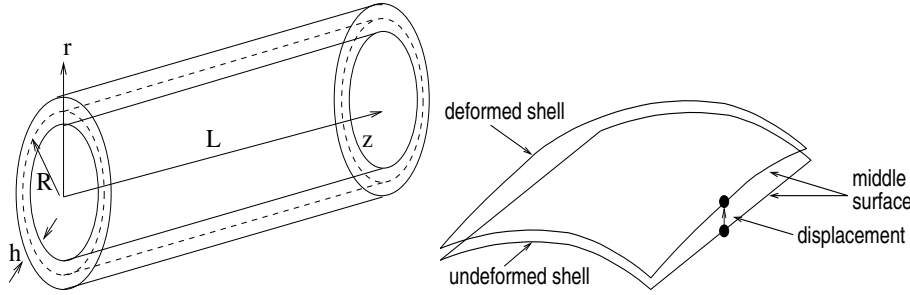- the state of stress is approximately plane.

FIG. 2.1. *Left: Cylindrical shell (reference configuration) with middle surface radius R and shell thickness h. Right: Deformed shell.*

The weak formulation, describing the variation of the strain energy density function, depends on the change of metric and the change of curvature tensors of the surface. The change of metric tensor captures the stretching of the surface and the change of curvature tensor captures the bending effects. The weak formulation of the Koiter shell describes variation of the energy that is due to stretching and bending of the shell.

Denote by $\boldsymbol{\xi}(z) = (\xi_z(z), \xi_r(z))$ the displacement of the middle surface at z (see Figure 2.1), where $\xi_z(z)$ and $\xi_r(z)$ denote the longitudinal and the radial component of the displacement, respectively. Here the axial symmetry of the problem has already been taken into account assuming that the displacement in the θ-direction is zero, and that nothing in the problem depends on θ. The change of metric and the change of curvature tensors for a cylindrical shell are given, respectively, by [11]

$$\boldsymbol{\gamma}(\boldsymbol{\xi}) = \begin{bmatrix} \xi_z' & 0 \\ 0 & R\xi_r \end{bmatrix}, \quad \boldsymbol{\varrho}(\boldsymbol{\xi}) = \begin{bmatrix} -\xi_r'' & 0 \\ 0 & \xi_r \end{bmatrix}.$$

Here $'$ denotes the derivative with respect to the longitudinal variable z. Introduce the following function space:

$$
\begin{aligned}
V_c &= H_0^1(0, L) \times H_0^2(0, L) \\
&= \big\{ (\xi_z, \xi_r) \in H^1(0, L) \times H^2(0, L) : \xi_z(0) = \xi_z(L) = \xi_r(0) = \xi_r(L) = 0, \\
&\qquad \xi_r'(0) = \xi_r'(L) = 0 \big\}.
\end{aligned}
$$

Then the weak formulation of the linearly elastic cylindrical Koiter shell is given by the following: find $\boldsymbol{\eta} = (\eta_z, \eta_r) \in V_c$ such that

$$(2.1) \quad \frac{h}{2} \int_0^L \mathcal{A}\boldsymbol{\gamma}(\boldsymbol{\eta}) \cdot \boldsymbol{\gamma}(\boldsymbol{\xi}) R dz + \frac{h^3}{24} \int_0^L \mathcal{A}\boldsymbol{\varrho}(\boldsymbol{\eta}) \cdot \boldsymbol{\varrho}(\boldsymbol{\xi}) R dz = \int_0^L \boldsymbol{f} \cdot \boldsymbol{\xi} R dz, \quad \boldsymbol{\xi} \in V_c,$$

where $\cdot$ denotes the scalar product

(2.2) $$A \cdot B := \mathrm{Tr}\left(AB^T\right), \quad A, B \in M_2(\mathbb{R}) \cong \mathbb{R}^4.$$

Here $\boldsymbol{f}$ is the surface density of the force applied to the shell, and $\mathcal{A}$ is the elasticity tensor given by [11]

$$\mathcal{A}\mathbf{E} = \frac{4\lambda\mu}{\lambda + 2\mu}(\mathbf{A}^c \cdot \mathbf{E})\mathbf{A}^c + 4\mu\mathbf{A}^c\mathbf{E}\mathbf{A}^c, \quad \mathbf{E} \in \mathrm{Sym}\left(\mathbb{R}^2\right), \quad \text{with}$$

$$\mathbf{A}_c = \begin{bmatrix} 1 & 0 \\ 0 & R^2 \end{bmatrix}, \quad \mathbf{A}^c = \begin{bmatrix} 1 & 0 \\ 0 & \frac{1}{R^2} \end{bmatrix},$$

where λ and μ are the Lamé constants. Written in terms of the displacement, the weak formulation reads

$$\frac{h}{2}\int_0^L \left(\frac{4\mu\lambda}{\lambda + 2\mu}\left(\eta_z' + \frac{1}{R}\eta_r\right) \cdot \left(\xi_z' + \frac{1}{R}\xi_r\right) + 4\mu\left(\eta_z'\xi_z' + \frac{1}{R^2}\eta_r\xi_r\right)\right) dz$$

$$+ \frac{h^3}{24}\int_0^L \left(\frac{4\mu\lambda}{\lambda + 2\mu}\left(-\eta_r'' + \frac{1}{R^2}\eta_r\right) \cdot \left(-\xi_r'' + \frac{1}{R^2}\xi_r\right) + 4\mu\left(\eta_r''\xi_r'' + \frac{1}{R^4}\eta_r\xi_r\right)\right) dz$$

$$= \int_0^L (f_z\xi_z + f_r\xi_r)dz \quad \forall(\xi_z, \xi_r) \in V_c.$$

Using the following relationships between the Lamé constants and Young's modulus of elasticity E and the Poisson ratio σ

$$\frac{2\mu\lambda}{\lambda + 2\mu} + 2\mu = 4\mu\frac{\lambda + \mu}{\lambda + 2\mu} = \frac{E}{1 - \sigma^2}, \quad \frac{2\mu\lambda}{\lambda + 2\mu} = 4\mu\frac{\lambda + \mu}{\lambda + 2\mu}\frac{1}{2}\frac{\lambda}{\lambda + \mu} = \frac{E}{1 - \sigma^2}\sigma,$$

the elasticity tensor $\mathcal{A}$ reads

$$\mathcal{A}\mathbf{E} = \frac{2E\sigma}{1 - \sigma^2}(\mathbf{A}^c \cdot \mathbf{E})\mathbf{A}^c + \frac{2E}{1 + \sigma}\mathbf{A}^c\mathbf{E}\mathbf{A}^c, \quad \mathbf{E} \in \mathrm{Sym}\left(\mathbb{R}^2\right).$$

From here we get the weak formulation (2.1) as

$$h\int_0^L \left(\frac{E\sigma}{1 - \sigma^2}\left(\eta_z' + \frac{1}{R}\eta_r\right)\left(\xi_z' + \frac{1}{R}\xi_r\right) + \frac{E}{1 + \sigma}\left(\eta_z'\xi_z' + \frac{1}{R^2}\eta_r\xi_r\right)\right) dz$$

$$+ \frac{h^3}{12}\int_0^L \left(\frac{E\sigma}{1 - \sigma^2}\left(-\eta_r'' + \frac{1}{R^2}\eta_r\right)\left(-\xi_r'' + \frac{1}{R^2}\xi_r\right) + \frac{E}{1 + \sigma}\left(\eta_r''\xi_r'' + \frac{1}{R^4}\eta_r\xi_r\right)\right) dz$$

$$= \int_0^L (f_z\xi_z + f_r\xi_r)dz, \quad (\xi_z, \xi_r) \in V_c.$$

(2.3)

The terms multiplying $h/2$ account for the stored energy density due to stretching (membrane effects) and the terms multiplying $h^3/12$ account for the stored energy density due to bending (flexural shell effects). Integration by parts gives rise to the static equilibrium equations. Written in differential form they read

(2.4)
$$-\frac{hE}{1 - \sigma^2}\left(\eta_z'' + \sigma\frac{1}{R}\eta_r'\right) = f_z,$$

$$\frac{hE}{R(1 - \sigma^2)}\left(\sigma\eta_z' + \frac{\eta_r}{R}\right) + \frac{h^3E}{12(1 - \sigma^2)}\left(\eta_r'''' - 2\sigma\frac{1}{R^2}\eta_r'' + \frac{1}{R^4}\eta_r\right) = f_r.$$

THE LINEARLY ELASTIC CYLINDRICAL KOITER SHELL MODEL

We employ these equations to study the response of arteries to pulsatile blood flow. For this purpose, we assume that the in vivo arteries are *prestretched* under internal pressure load, that the arterial walls are *longitudinally tethered*, and that the *longitudinal displacement is negligible* [38, 42].

The assumption that the longitudinal displacement is negligible has been justified in [38]. More precisely, in [38] we considered the equations of *three-dimensional* linear elasticity to model the vessel wall, coupled with the Navier–Stokes equations for a viscous, incompressible fluid to model the flow of blood in cylindrical geometry. In addition, we assumed that the "thickness" h of the structure (the radial dimension of the three-dimensional elastic body) is less than or comparable to the radius of the domain occupied by the fluid, i.e., $h/R \leq 1$ (this includes the scenario $h/R \ll 1$ considered in this manuscript). Starting from the assumption that both the radial and longitudinal displacement of the three-dimensional structure are nonzero, we showed that the effective model obtained by considering small aspect ratio $\epsilon = R/L$ embodies negligible longitudinal displacement of the structure.

Taking this into account we emply here the equations of a linearly elastic cylindrical Koiter shell model with negligible longitudinal displacement:

$$(2.5) \qquad \boxed{\left(\frac{hE}{R(1-\sigma^2)} + p_{\text{ref}} \right) \frac{\eta_r}{R} + \frac{h^3 E}{12(1-\sigma^2)} \left(\eta_r'''' - 2\sigma \frac{1}{R^2} \eta_r'' + \frac{1}{R^4} \eta_r \right) = f_r.}$$

This is obtained from the weak formulation (2.3), assuming $\eta_z = 0$, and the test space

$$V_c^0 := V_c \cap \{\xi_z = 0\}.$$

In order to include the fact that the reference configuration is prestressed at reference pressure p_{ref}, and that the arterial walls are viscoelastic, we study the stress-strain relationship corresponding to the Koiter shell model and modify it to include these two effects. This is presented next.

2.2. The linearly viscoelastic Koiter shell model. The stress-strain relationship is given by the "stress resultant," which relates the internal force with the change of metric tensor, and the "stress couples," which describe the bending moments in terms of the change of curvature tensor [20]. As noted by Koiter in his original paper [31], the stress resultant and the stress couples can be obtained from (2.1) as gradients of the stored energy function, given by the integrand on the left-hand side of (2.1), with respect to the middle surface strains and changes of curvature. Following this approach one obtains

- *stress resultant (or the internal force) for the elastic Koiter shell*

$$(2.6) \qquad N := \frac{h}{2} \mathcal{A} \boldsymbol{\gamma}(\boldsymbol{\eta}) = \frac{h}{2} \begin{bmatrix} \frac{2E\sigma}{1-\sigma^2} \frac{\eta_r}{R} & 0 \\ 0 & \frac{2E}{1-\sigma^2} \frac{\eta_r}{R^3} \end{bmatrix},$$

- *stress couples (bending moment) for the elastic Koiter shell*

$$(2.7)$$
$$M := \frac{h^3}{24} \mathcal{A} \boldsymbol{\varrho}(\boldsymbol{\eta}) = \frac{h^3}{24} \begin{bmatrix} -\frac{2E}{1-\sigma^2} \eta_r'' + \frac{2E\sigma}{1-\sigma^2} \frac{\eta_r}{R^2} & 0 \\ 0 & \frac{2E}{1-\sigma^2} \frac{u_r}{R^4} - \frac{2E\sigma}{1-\sigma^2} \frac{1}{R^2} \eta_r'' \end{bmatrix}.$$

At this point we also introduce the effects of prestress by defining the stress resultant N_{ref} that relates the reference pressure p_{ref} with the circumferential strain [17, 34, 35]

$$(2.8) \qquad \frac{h}{2} N_{\text{ref}} = hR \mathbf{A}^c \begin{bmatrix} 0 & 0 \\ 0 & p_{ref} \frac{R}{h} \eta_r \end{bmatrix} \mathbf{A}^c$$

so that the total stress resultant, including the effects of prestress, reads
- *stress resultant for the prestressed elastic Koiter shell*

$$(2.9) \qquad N = \frac{h}{2}\mathcal{A}\boldsymbol{\gamma}(\boldsymbol{\eta}) + \frac{h}{2}N_{\text{ref}}.$$

We focus now on introducing the viscous effects to the linearly elastic, prestressed cylindrical Koiter shell model. For this purpose assume that the displacement is not only a function of position z but also a function of time: $\boldsymbol{\eta} = \boldsymbol{\eta}(z,t)$ and that the velocity of the displacement is linearly proportional to the stress as described in (1.1). Employing the Kelvin–Voigt model (1.1) to describe this viscoelastic behavior one writes the constitutive relations in which the stress is linearly proportional to the strain plus the time-derivative of strain [20]. For the linearly viscoelastic Koiter shell model we define
- *stress resultant for the viscoelastic prestressed Koiter shell*

$$(2.10) \qquad N := \frac{h}{2}\mathcal{A}\boldsymbol{\gamma}(\boldsymbol{\eta}) + \frac{h}{2}\mathcal{B}\boldsymbol{\gamma}(\dot{\boldsymbol{\eta}}) + \frac{h}{2}N_{\text{ref}},$$

- *stress couples for the viscoelastic Koiter shell*

$$(2.11) \qquad M := \frac{h^3}{24}\mathcal{A}\boldsymbol{\varrho}(\boldsymbol{\eta}) + \frac{h^3}{24}\mathcal{B}\boldsymbol{\varrho}(\dot{\boldsymbol{\eta}}),$$

where $\mathcal{B}$ is given by

$$\mathcal{B}\mathbf{E} = \frac{4\lambda_v\mu_v}{\lambda_v + 2\mu_v}(\mathbf{A}^c \cdot \mathbf{E})\mathbf{A}^c + 4\mu_v\mathbf{A}^c\mathbf{E}\mathbf{A}^c, \quad \mathbf{E} \in \mathrm{Sym}\,(\mathbb{R}^2),$$

with μ_v and λ_v corresponding to the viscous counterpart of the Lamé constants μ and λ. With these constitutive relations we now define the weak formulation of the linearly viscoelastic prestressed Koiter shell model by the following: for each $t > 0$ find $\eta(t) \in V_c$ such that $\forall \boldsymbol{\xi}(t) \in V_c$

$$\frac{h}{2}\int_0^L \left(N_{\text{ref}} + \mathcal{A}\boldsymbol{\gamma}(\boldsymbol{\eta}) + \mathcal{B}\boldsymbol{\gamma}(\dot{\boldsymbol{\eta}})\right) \cdot \boldsymbol{\gamma}(\boldsymbol{\xi})Rdz + \frac{h^3}{24}\int_0^L \left(\mathcal{A}\boldsymbol{\varrho}(\boldsymbol{\eta}) + \mathcal{B}\boldsymbol{\varrho}(\dot{\boldsymbol{\eta}})\right) \cdot \boldsymbol{\varrho}(\boldsymbol{\xi})Rdz$$

$$(2.12) \qquad + \rho_w h\int_0^L \frac{\partial^2 \boldsymbol{\eta}}{\partial t^2} \cdot \boldsymbol{\xi} = \int_0^L \boldsymbol{f} \cdot \boldsymbol{\xi}Rdz,$$

where $\dot{\boldsymbol{\eta}}$ denotes the time-derivative. Written in terms of the displacement, after employing the notation

$$(2.13) \qquad C_v := \frac{2\lambda_v\mu_v}{\lambda_v + 2\mu_v} + 2\mu_v, \quad D_v := \frac{2\lambda_v\mu_v}{\lambda_v + 2\mu_v},$$

the weak formulation of the linearly viscoelastic prestressed Koiter shell model reads

$$\int_0^L f_r\xi_r dz = \rho_w h\int_0^L \frac{\partial^2 \eta_r}{\partial t^2}\xi_r + h\int_0^L \left(\left(\frac{E}{1-\sigma^2} + p_{\text{ref}}\frac{R}{h}\right)\frac{1}{R}\eta_r + C_v\frac{1}{R}\frac{\partial \eta_r}{\partial t}\right)\frac{\xi_r}{R}dz$$

$$+ \frac{h^3}{12}\int_0^L \left(\left(\frac{E\sigma}{1-\sigma^2}\left(-\frac{\partial^2 \eta_r}{\partial z^2} + \frac{\eta_r}{R^2}\right) + D_v\left(-\frac{\partial^3 \eta_r}{\partial t\partial z^2} + \frac{1}{R^2}\frac{\partial \eta_r}{\partial t}\right)\right)\left(-\frac{\partial^2 \xi_r}{\partial z^2} + \frac{\xi_r}{R^2}\right)\right.$$

$$+ \left(\frac{E}{1+\sigma}\frac{\partial^2 \eta_r}{\partial z^2} + (C_v - D_v)\frac{\partial^3 \eta_r}{\partial t\partial z^2}\right)\frac{\partial \xi_r}{\partial z^2} + \left.\left(\frac{E}{1+\sigma}\frac{1}{R^2}\eta_r + (C_v - D_v)\frac{1}{R^2}\frac{\partial \eta_r}{\partial t}\right)\frac{\xi_r}{R^2}\right)dz$$

$\forall \boldsymbol{\xi}(t) \in V_c^0$. Integration by parts gives rise to the equilibrium equation

(2.14)

$$\boxed{f_r = \rho_w h \frac{\partial^2 \eta_r}{\partial t^2} + C_0 \eta_r - C_1 \frac{\partial^2 \eta_r}{\partial z^2} + C_2 \frac{\partial^4 \eta_r}{\partial z^4} + D_0 \frac{\partial \eta_r}{\partial t} - D_1 \frac{\partial^3 \eta_r}{\partial t \partial z^2} + D_2 \frac{\partial^5 \eta_r}{\partial t \partial z^4}},$$

THE LINEARLY VISCOELASTIC CYLINDRICAL PRESTRESSED KOITER SHELL MODEL WITH ZERO LONGITUDINAL DISPLACEMENT

where ρ_w denotes the shell density (see Table 4.1) and

(2.15)

$$C_0 = \frac{h}{R^2} \frac{E}{1-\sigma^2} \left(1 + \frac{h^2}{12R^2} \right) + \frac{p_{\text{ref}}}{R}, \quad C_1 = 2 \frac{h^3}{12R^2} \frac{E\sigma}{1-\sigma^2}, \quad C_2 = \frac{h^3}{12} \frac{E}{1-\sigma^2},$$

$$D_0 = \frac{h}{R^2} C_v \left(1 + \frac{h^2}{12R^2} \right), \qquad\qquad D_1 = 2 \frac{h^3}{12R^2} D_v, \qquad D_2 = \frac{h^3}{12} C_v.$$

We use this equation to model the motion of compliant arterial walls interacting with the time-dependent fluid flow driven by the pulsatile inlet and outlet pressure data. To simplify notation, from this point on in this manuscript we will be using η to denote the radial displacement η_r.

3. Fluid-structure interaction: The three-dimensional model. In medium to large arteries blood can be modeled as an incompressible, Newtonian viscous fluid. We will be assuming that the viscosity of blood is constant, utilizing the data from biomedical literature (see, e.g., [21, 39, 44]), providing the viscosity coefficient $\mu_F = 3500$ kg/ms. The Navier–Stokes equations for a viscous, incompressible fluid have been well accepted as a model for blood flow in medium-to-large arteries. Assuming cylindrical geometry and axially symmetric flow, the fluid velocity $\boldsymbol{v}(r,z,t) = (v_r(r,z,t), v_z(r,z,t))$ and pressure $p(r,z,t)$ satisfy

(3.1) $\quad \rho_F \left\{ \dfrac{\partial v_r}{\partial t} + v_r \dfrac{\partial v_r}{\partial r} + v_z \dfrac{\partial v_r}{\partial z} \right\} - \mu_F \left(\dfrac{\partial^2 v_r}{\partial r^2} + \dfrac{\partial^2 v_r}{\partial z^2} + \dfrac{1}{r} \dfrac{\partial v_r}{\partial r} - \dfrac{v_r}{r^2} \right) + \dfrac{\partial p}{\partial r} = 0,$

(3.2) $\quad\quad \rho_F \left\{ \dfrac{\partial v_z}{\partial t} + v_r \dfrac{\partial v_z}{\partial r} + v_z \dfrac{\partial v_z}{\partial z} \right\} - \mu_F \left(\dfrac{\partial^2 v_z}{\partial r^2} + \dfrac{\partial^2 v_z}{\partial z^2} + \dfrac{1}{r} \dfrac{\partial v_z}{\partial r} \right) + \dfrac{\partial p}{\partial z} = 0,$

(3.3) $\quad\quad\quad\quad\quad\quad\quad\quad\quad\quad\quad\quad\quad\quad\quad \dfrac{\partial v_r}{\partial r} + \dfrac{\partial v_z}{\partial z} + \dfrac{v_r}{r} = 0.$

Here ρ_F is the fluid density and μ_F is the fluid dynamic viscosity coefficient, where the subscript F stands for the fluid quantities. The Navier–Stokes equations hold in the cylindrical domain

(3.4) $\quad\quad \Omega(t) = \left\{ x \in \mathbb{R}^3; x = (r \cos \vartheta, r \sin \vartheta, z), \ r < R + \eta(z,t), \ 0 < z < L \right\}$

bounded by the viscoelastic lateral boundary

$$\Sigma(t) = \left\{ ((R(z) + \eta(t,z)) \cos \theta, (R(z) + \eta(t,z)) \sin \theta, z) \in \mathbb{R}^3 : \theta \in (0, 2\pi), z \in (0, L) \right\}.$$

See Figure 3.1. The reference configuration corresponds to that of a straight cylinder with radius R and length L. (The same results can be obtained for a cylinder with a slowly varying radius $R(z)$ under the assumption that $R'(z) < \epsilon$ [47].) The following inlet ($z = 0$) and outlet ($z = L$) boundary data lead to a well-defined problem:
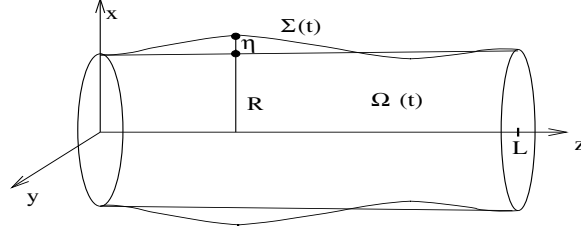
FIG. 3.1. *Deformed domain* $\Omega(t)$.

1. The dynamic pressure is prescribed at both ends:

$$(3.5) \qquad p + \rho(v_z)^2/2 = P_{0,L}(t) + p_{\text{ref}} \text{ at } z = 0, L.$$

2. The fluid enters and leaves the tube parallel to the axis of symmetry, with zero displacement:

$$(3.6) \qquad v_r = 0, \quad \eta = 0 \text{ at } z = 0, L.$$

3. The tube is clamped so that

$$(3.7) \qquad \frac{\partial \eta}{\partial z} = 0 \text{ at } z = 0, L.$$

In the reduced model (see section 4), the zero displacement condition is relaxed. This is typical for reduced models where the boundary layer phenomena near the edges with high stress concentrations are lost [8].

Initially, the fluid and the wall are assumed to be at rest, with zero displacement from the reference configuration:

$$(3.8) \qquad \boldsymbol{v} = 0, \quad \eta = 0, \quad \frac{\partial \eta}{\partial t} = 0.$$

These initial and boundary conditions describe well our experimental set up, described in section 7.

The coupling between the fluid flow and vessel wall dynamics is performed via the following kinematic and dynamic lateral boundary conditions [9]:

- The kinematic condition requiring continuity of velocity:

$$(3.9) \qquad v_r(R + \eta(z,t), z, t) = \frac{\partial \eta(z,t)}{\partial t}, \quad v_z(R + \eta(z,t), z, t) = 0.$$

- The dynamic condition requiring balance of forces (the contact force of the fluid is counterbalanced by the contact force of the wall):

$$(3.10) \qquad f_r = [(p - p_{\text{ref}})\mathbf{I} - 2\mu_F D(\boldsymbol{v})] \, \boldsymbol{n} \cdot \boldsymbol{e}_r \left(1 + \frac{\eta}{R}\right) \sqrt{1 + (\partial_z \eta)^2},$$

where f_r is given by the viscoelastic shell model (2.14). The right-hand side of (3.10) describes the contact force of the fluid, where $D(\boldsymbol{v})$ is the symmetrized gradient of velocity, defined in (3.12), $\boldsymbol{n}$ is the vector normal to the deformed boundary $\Sigma(t)$, and $\boldsymbol{e}_r$ is the radial unit vector.

See [9] for more details.

Thus, the complete fluid-structure interaction problem consists of solving the fluid equations (3.1)–(3.3) on the domain $\Omega(t)$ defined by (3.4) with a moving boundary $\Sigma(t)$, satisfying the initial and boundary data given by (3.5)–(3.10) where the contact force of the structure f_r is given by (2.14).

3.1. Weak formulation. To derive a weak formulation of the fluid-structure interaction problem we take the standard approach: multiply the fluid equations by a test function, integrate by parts, and take into account the initial and boundary conditions to obtain the integral form of the problem. For that purpose, introduce the following test spaces.

DEFINITION 3.1 (the test spaces). *Let*

(3.11)

$$V(\Omega(t)) = \{\varphi = \varphi_r \boldsymbol{e}_r + \varphi_z \boldsymbol{e}_z \in H^2(\Omega(t))^2 \mid \varphi_r(r, z) = \partial_z \varphi_r(r, z) = 0 \text{ at } z = 0, L,$$
$$\varphi_z(R + \gamma(z, t), z) = 0, \text{ and } \operatorname{div} \varphi = 0 \text{ in } \Omega(t) \text{ a.e.}\}.$$

For each $t \in [0, T]$, the test space is the space $H^1(0, T; V(\Omega(t)))$.

To specify the weak solution we introduce the spaces containing the candidates for the radial displacement and the velocity. They are deduced from the a priori solution estimates, presented in section 3.2.

DEFINITION 3.2 (the solution spaces).

- *The space Γ consists of all the functions*

$$\eta \in L^\infty(0, T; H^2(0, L)) \cap C^1([0, T]; L^2(0, L)) \cap C([0, T]; H^2(0, L))$$

  such that $\eta(t, 0) = \eta(t, L) = 0$, $\partial_z \eta(t, 0) = \partial_z \eta(t, L) = 0$, and $\eta(0, z) = \partial_t \eta(0, z) = 0$.

- *The space V consists of all the functions*

$$v = (v_r, v_z) \in L^2(0, T; H^1(\Omega(t))^2) \cap C([0, T]; L^2(\Omega(t))^2)$$

  such that $\operatorname{div} \boldsymbol{v} = 0$ in $\Omega(t) \times \mathbb{R}_+$, $v_r = 0$ for $z = 0, L$, and $\boldsymbol{v} = 0$ at $t = 0$.

To define the weak form recall that the symmetrized gradient of velocity $D(\varphi)$, defined for an axially symmetric vector valued function $\boldsymbol{\varphi} = \varphi_r \boldsymbol{e}_r + \varphi_z \boldsymbol{e}_z$, is given by

(3.12)
$$D(\boldsymbol{\varphi}) = \begin{pmatrix} \dfrac{\partial \varphi_r}{\partial r} & 0 & \dfrac{1}{2}\left(\dfrac{\partial \varphi_r}{\partial z} + \dfrac{\partial \varphi_z}{\partial r}\right) \\ 0 & \dfrac{\varphi_r}{r} & 0 \\ \dfrac{1}{2}\left(\dfrac{\partial \varphi_r}{\partial z} + \dfrac{\partial \varphi_z}{\partial r}\right) & 0 & \dfrac{\partial \varphi_z}{\partial z} \end{pmatrix}.$$

Define the matrix norm $| \cdot |$ through the scalar product

(3.13)
$$A \cdot B := \operatorname{Tr}\left(AB^T\right), \quad A, B \in \mathbb{R}^9.$$

DEFINITION 3.3. *A weak solution of problem* (3.1)–(3.10) *is a function* $(\eta, \boldsymbol{v}) \in \Gamma \times V$ *such that $\forall \varphi \in H^1(0, T; V(\Omega(t)))$ the following integral equation holds:*

$$2\mu_F \int_{\Omega(t)} D(v) \cdot D(\varphi) \, r dr dz + \rho \int_{\Omega(t)} \left\{\frac{\partial v}{\partial t} + (v(t)\nabla)v\right\} \varphi \, r dr dz$$

$$+ R \int_0^L \left\{ C_0 \eta \left.\varphi_r\right|_{R+\eta} + C_1 \frac{\partial \eta}{\partial z} \left.\frac{\partial \varphi_r}{\partial z}\right|_{R+\eta} + C_2 \frac{\partial^2 \eta}{\partial z^2} \left.\frac{\partial^2 \varphi_r}{\partial z^2}\right|_{R+\eta} \right.$$

(3.14) $$+ D_0 \frac{\partial \eta}{\partial t} \left.\varphi_r\right|_{R+\eta} + D_1 \frac{\partial^2 \eta}{\partial t \partial z} \left.\frac{\partial \varphi_r}{\partial z}\right|_{R+\eta} + D_2 \frac{\partial^3 \eta}{\partial t \partial z^2} \left.\frac{\partial^2 \varphi_r}{\partial z^2}\right|_{R+\eta} \right\} dz$$

$$+ R \rho_w h \int_0^L \frac{\partial^2 \eta}{\partial t^2} \varphi_r(R + \eta(t, z), z, t) \, dz = - \int_0^R \left\{ P_2(t) - \frac{\rho}{2}(v_z^2)|_{z=L} \right\} \varphi_z|_{z=L} r dr$$

$$+ \int_0^R \left\{ P_1(t) - \frac{\rho}{2}(v_z^2)|_{z=0} \right\} \varphi_z|_{z=0} r dr,$$

where $\Omega(t)$ is given by (3.4) and η and v_r are linked on $\Sigma(t)$ through (3.9).

Notice that the domain as well as the solution and test spaces depend on time. To get a global weak formulation one can use the a priori solution estimates, presented below, and define a global weak solution via a fixed point mapping, defined on a fixed, "fictitious" domain. This approach is used in [9] to define a global weak solution for a related fluid-structure interaction problem using the linearly elastic membrane equations to model the vessel walls. We do not pursue this approach here but continue with the derivation of the energy and a priori estimates.

3.2. The energy and a priori estimates. By replacing the test function with the fluid velocity and using the kinematic lateral boundary condition (3.9) one obtains the following proposition.

PROPOSITION 3.4 (energy equality). *Solution $(\eta, \boldsymbol{v})$ of problem (3.1)–(3.10) satisfies the following energy equality:*

$$\frac{\rho}{2}\frac{d}{dt}\int_{\Omega(t)}|\boldsymbol{v}|^2\,dV + \frac{\pi R}{2}\frac{d}{dt}\int_0^L\left\{C_0|\eta|^2 + C_1\left|\frac{\partial\eta}{\partial z}\right|^2 + C_2\left|\frac{\partial^2\eta}{\partial z^2}\right|^2\right\}dz$$

$$+\frac{\pi R}{2}\rho_w h\frac{d}{dt}\int_0^L\left|\frac{\partial\eta}{\partial t}\right|^2\,dz + \pi R\int_0^L\left\{D_0\left|\frac{\partial\eta}{\partial t}\right|^2 + D_1\left|\frac{\partial^2\eta}{\partial t\partial z}\right|^2 + D_2\left|\frac{\partial^3\eta}{\partial t\partial z^2}\right|^2\right\}dz$$

$$(3.15)\quad + 2\mu_F\|D(\boldsymbol{v})\|_{L^2(\Omega(t))}^2 = -\int_0^R P_2(t)v_z(t,r,L)\,rdr + \int_0^R P_1(t)v_z(t,r,0)\,rdr,$$

with $v_r(t, R+\eta, z) = \frac{\partial\eta}{\partial t}(t,z)$ and $v_z(t, R+\eta, z) = 0$ on $(0, L) \times (0, T)$.

To obtain the a priori estimates and the correct scales for the problem, we introduce the nondimensional time

$$(3.16)\qquad\qquad\qquad\qquad \hat{t} := \omega t.$$

The characteristic frequency ω will be specified later in (3.21). The choice of ω determines the time-scale for the natural oscillations of the structure in terms of the inlet and outlet pressure data. As it will be seen later, the quantity $L\omega$ corresponds to the "sound speed" of the natural oscillations of the structure, and the choice of ω given in (3.21) gives rise to the structure sound speed reported in Fung [21]. From now on we will be working with the nondimensional time $\hat{t}$ but will drop the "hat" notation for simplicity. Whenever physical time t is used, this will be explicitly specified.

Take the rescaled time into account and integrate the energy equality with respect to time to obtain

$$(3.17)\qquad \frac{\rho\omega}{2}\int_{\Omega(t)}|\boldsymbol{v}|^2\,dV + \frac{\pi R\omega}{2}\int_0^L\left\{C_0|\eta|^2 + C_1\left|\frac{\partial\eta}{\partial z}\right|^2 + C_2\left|\frac{\partial^2\eta}{\partial z^2}\right|^2\right\}dz$$

$$+\frac{\pi R\omega^3}{2}\rho_w h\int_0^L\left|\frac{\partial\eta}{\partial t}\right|^2\,dz + \pi R\omega^2\int_0^t\int_0^L\left\{D_0\left|\frac{\partial\eta}{\partial t}\right|^2 + D_1\left|\frac{\partial^2\eta}{\partial t\partial z}\right|^2 + D_2\left|\frac{\partial^3\eta}{\partial t\partial z^2}\right|^2\right\}dzd\tau$$

$$+2\mu_F\int_0^t\|D(\boldsymbol{v})\|_{L^2(\Omega(\tau))}^2\,d\tau = -\int_0^t\int_0^R(P_2(\tau)v_z(\tau,r,L) - P_1(\tau)v_z(\tau,r,0))\,rdrd\tau.$$

By estimating the right-hand side in a manner similar to the estimates in [9] and [6]

one obtains

(3.18) $\dfrac{\rho\omega}{2}\|\boldsymbol{v}\|^2_{L^2(\Omega(t))} + \pi\omega^3\rho_w hR\,\|\partial_t\eta\|^2 + \dfrac{\pi\omega RC_0}{2}\|\eta\|^2$

$$\leq \dfrac{16\pi LR\omega}{C_0}\left(\sup_{z,t}|\hat{p}|^2 + \left(\sup_z\int_0^t|\partial_t\hat{p}|d\tau\right)^2\right) + \dfrac{8T\pi R^2}{\rho\omega L}\int_0^t|A(\tau)|^2 d\tau,$$

where

(3.19) $$A(t) = P_L(t) - P_0(t), \quad \hat{p}(t) = \dfrac{A(t)}{L}z + P_0(t),$$

and $T > 0$ denote the physical time such that

(3.20) $$T \leq \dfrac{1}{4}\dfrac{R\sqrt{\rho_w hC_0}}{\|p\|_\infty}.$$

For example, for $p_{\text{ref}} = 0$, this inequality reads $T \leq 1/[4(1-\sigma^2)]h\sqrt{E\rho_w}/\|p\|_\infty$.

This is the point were we define the frequency ω. Choose ω so that the contribution of all the terms involving the pressure data have the same weight. Namely, choose ω so that the time-scale of the captured oscillations is determined by the pressure drop $A(t)$, the inlet and outlet maximum pressure, and by the time-average of the steepness of the pressure front $\partial_t\hat{p}$ to obtain

(3.21) $$\omega = \dfrac{1}{L}\sqrt{\dfrac{RC_0}{2\rho}}.$$

This choice of ω gives rise to the sound speed of the waves in the "structure" ωL which is exactly the sound speed reported by Fung in [21]. After taking this form of ω into account, and after dividing (3.18) by ω, we obtain the following energy inequality from which the a priori estimates will follow.

PROPOSITION 3.5. *Weak solution* $(\eta, \boldsymbol{v})$ *satisfies*

$$\dfrac{\rho}{2}\|\boldsymbol{v}\|^2_{L^2(\Omega(t))} + \pi\omega^2\rho_w hR\,\|\partial_t\eta\|^2 + \dfrac{\pi R}{2}C_0\|\eta\|^2 \leq \dfrac{16\pi LR}{C_0}\mathcal{P}^2, \text{ where}$$

(3.22) $$\mathcal{P}^2 := \sup_{z,t}|\hat{p}|^2 + \left(\sup_z\int_0^t|\hat{p}_t|d\tau\right)^2 + T\int_0^t|A(\tau)|^2.$$

Using this result we obtain the a priori estimates for the L^2-norms of the fluid velocity, the displacement, and the time-derivative of the displacement.

LEMMA 3.6. *Weak solution* $(\eta, \boldsymbol{v})$ *satisfies the following a priori estimates:*

$$\dfrac{1}{L}\|\eta(t)\|^2_{L^2(0,L)} \leq \dfrac{32}{C_0^2}\mathcal{P}^2, \quad \dfrac{1}{L}\,\|\partial_t\eta(t)\|^2_{L^2(0,L)} \leq \dfrac{16}{\rho_W\omega^2 hC_0}\mathcal{P}^2,$$

$$\dfrac{1}{LR^2\pi}\|\boldsymbol{v}\|^2_{L^2(\Omega(t))} \leq \dfrac{32}{\rho_F RC_0}\mathcal{P}^2,$$

$$\int_0^t\left\{\|\partial_r v_r\|^2_{L^2(\Omega(\tau))} + \left\|\dfrac{v_r}{r}\right\|^2_{L^2(\Omega(\tau))} + \|\partial_z v_z\|^2_{L^2(\Omega(\tau))}\right\}d\tau \leq \dfrac{4\pi R^2}{\mu_F}\sqrt{\dfrac{2}{\rho_F RC_0}}\mathcal{P}^2,$$

$$\int_0^t\left\{\|\partial_r v_z\|^2_{L^2(\Omega(\tau))} + \|\partial_z v_r\|^2_{L^2(\Omega(\tau))}\right\}d\tau \leq \dfrac{4R^2}{\mu_F}\sqrt{\dfrac{2}{\rho RC_0}}\mathcal{P}^2.$$

Furthermore, we obtain the following estimates for the functions describing the viscoelastic behavior of the structure.

COROLLARY 3.7.   *The following estimates hold for the viscoelastic thin shell model:*

$$\frac{\omega}{L} \int_0^t \left\| \frac{\partial \eta}{\partial t} \right\|_{L^2}^2 d\tau \le \frac{32}{C_0 D_0} \mathcal{P}^2, \quad \frac{\omega}{L} \int_0^t \left\| \frac{\partial^2 \eta}{\partial t \partial z} \right\|_{L^2}^2 d\tau \le \frac{32}{C_0 D_1} \mathcal{P}^2,$$

$$\frac{\omega}{L} \int_0^t \left\| \frac{\partial^3 \eta}{\partial t \partial^2 z} \right\|_{L^2}^2 d\tau \le \frac{32}{C_0 D_0} \mathcal{P}^2,$$

where $\mathcal{P}$ is given by (3.22), *and ω by* (3.21).

The a priori estimates obtained in this section will be used to derive the reduced model presented below.

4. Fluid-structure interaction: A reduced model. We proceed by deriving a closed, effective, reduced model, approximating the full, original axially symmetric problem to the ϵ^2-accuracy.

We begin by considering (3.1)–(3.3) written in nondimensional form. The scalings for the dependent variables $\boldsymbol{v}$ and η are obtained from the a priori estimates presented in Lemma 3.6

$$(4.1) \qquad \boldsymbol{v} = V\tilde{\boldsymbol{v}}, \text{ where } 2V = \frac{\mathcal{P}}{\sqrt{\rho_F}} \left(\frac{hE}{R(1-\sigma^2)} + p_{\text{ref}} \right)^{-\frac{1}{2}},$$

$$(4.2) \qquad \eta = \Xi\tilde{\eta}, \text{ where } 2\Xi = \mathcal{P}R \left(\frac{hE}{R(1-\sigma^2)} + p_{\text{ref}} \right)^{-1}.$$

Consider $p = C_p \tilde{p}$, where C_p will be determined later; see (4.11). The nondimensional independent variables $\tilde{r}$, $\tilde{z}$, and $\tilde{t}$ are introduced via

$$(4.3) \qquad r = R\tilde{r}, \quad z = L\tilde{z}, \quad t = \frac{1}{\omega}\tilde{t}, \text{ where } \omega = \frac{1}{L}\sqrt{\frac{1}{\rho_F} \left(\frac{hE}{R(1-\sigma^2)} + p_{\text{ref}} \right)}.$$

At this point we could continue by performing singular perturbation analysis of the rescaled system (3.1)–(3.10), (2.14). As in [9], we would find a two-dimensional reduced free-boundary problem approximating the initial problem to the ϵ^2-accuracy. This problem involves a hydrostatic approximation of the pressure, and it is usually written as an analogue of the shallow water system. Elimination of the radial component of the velocity leads to a nonlocal degenerate term. The resulting equations are too complex to be used in the calculation of the solution, and simplifications involving an ad hoc axial velocity profile are typically considered in the literature. Typically considered v_z-profiles are in the form of a product of an unknown function of z and t and a generalized Poiseuille profile in r (see, e.g., [44]). The resulting variant of the shallow water equations is then closed, but the closure hypothesis could introduce an error of order 1.

In order to find a closure that results from the problem itself and gives rise to an ϵ^2-approximation of the full three-dimensional axially symmetric problem, we are going to use homogenization theory [4]. Homogenization theory is used to find effective equations for nonhomogeneous flows. For porous media problems homogenization theory can be applied when (a) the pore size (characteristic size of the fluid region free of another phase) is smaller than the characteristic length of the macroscopic

problem (here, vessel diameter) or (b) the pore includes a large number of molecules to be considered as continuum [28].

At a first glance using this approach in our setting is pointless. A simple averaging of the equations for the fluid phase over the cross-section of the vessel should provide a good approximation. Unfortunately, as remarked above, this approach leads to a problem that is not closed and might ultimately give rise to the errors of order 1. On the other hand, we know how to obtain closed models related to nonlinear filtration laws in rigid periodic porous media by homogenization [36, 37]. In rigid periodic porous media the expansions are of lower order of precision, but the resulting models are closed. It was shown in [36, 37] that in this case it is possible to link the homogenized equations with the nonlinear algebraic relations between the pressure gradient and the velocity (Forchheimer's filtration law), found in experiments. In a similar way, Robertson and Sequeira [46] obtained a closed model for blood flow in rigid wall tubes by replacing the averaged momentum equation with a variant of Forchheimer's law, and no closure assumption was needed to derive a closed system.

In our case we are concerned with viscoelastic walls. How do we link the flow of blood through viscoelastic arteries with the filtration through porous media? Due to the uniform bound on the maximal value of the radial displacement, obtained in section 3.2, our artery can be placed into a rectangle with the length of order 1 and of small width ϵ. By repeating periodically this geometry in the radial direction, we get a network of parallel, long, and narrow tubes, with no cross-flow from one horizontal tube to another. This is one of the simplest porous media which one can imagine. It is not a rigid but a *deformable* porous medium, just as are the domains in Biot's theories of deformable porous media. All results that are valid for deformable porous media are also valid in our situation. Motivated by the results from [36] and [37], where closed effective porous medium equations were obtained using homogenization techniques, we set up a problem that mimics a similar scenario.

Introduce $y = \frac{1}{\epsilon}\tilde{z}$ and assume periodicity in y of the domain and of the velocity and the pressure. Furthermore, recalling that we have a narrow long tube with $\tilde{r} = \frac{1}{R}r = \frac{1}{\epsilon}\frac{r}{L}$, assume periodicity in the radial direction thereby forming a network of a large number of strictly separated, parallel tubes. Follow the approach first presented in [9]. In [9] a closed, reduced model was derived in the case when the vessel walls were approximated by a linearly elastic membrane equations. In the present manuscript, the introduction of a linearly viscoelastic Koiter shell model introduces minor differences in the derivation of the reduced model. Thus, we present only the main steps in the derivation and omit the details which can be found in [9].

Following standard approach in homogenization theory [28, 4], we look for the unknown functions that explicitly depend on the "slow variables" r and $\tilde{z}$ as well as on the "fast variables" r/ϵ and $\tilde{z}/\epsilon =: y$. In our problem the slow and fast variables are related through $z = L\tilde{z} := L\epsilon y = Ry$, $r = R\tilde{r}$. Thus, we look for the functions

$$(4.4) \quad \tilde{\boldsymbol{v}} = \tilde{\boldsymbol{v}}(\tilde{t}, r, r/\epsilon, \tilde{z}, \tilde{z}/\epsilon), \quad \tilde{\eta} = \tilde{\eta}(\tilde{t}, r, r/\epsilon, \tilde{z}, \tilde{z}/\epsilon), \quad \text{and } \tilde{p} = \tilde{p}(\tilde{t}, r, r/\epsilon, \tilde{z}, \tilde{z}/\epsilon)$$

that are 1-periodic in $y = \tilde{z}/\epsilon$ and r/ϵ and satisfy the Navier–Stokes equations (3.1)–(3.3). Keeping both the fast and the slow variables in the derivation of the equations, namely keeping r, r/ϵ, $\tilde{z}$, and y in the problem, will help us determine the proper scaling for the pressure and lead us to a closed, reduced effective model.

Expand the functions in (4.4) in terms of the small parameter ϵ

$$(4.5)$$
$$\boldsymbol{v} = V\left\{\tilde{\boldsymbol{v}}^0 + \epsilon\tilde{\boldsymbol{v}}^1 + \cdots\right\}, \quad \eta = \Xi\left\{\tilde{\eta}^0 + \epsilon\tilde{\eta}^1 + \cdots\right\}, \quad p = C_p\left\{\tilde{p}^0 + \epsilon\tilde{p}^1 + \cdots\right\}$$

Parameters	Aorta/iliacs	Latex Tube
Char. radius $R(\text{m})$	0.006-0.012 [44]	0.011
Char. length $L(\text{m})$	0.065-0.2 [14]	0.34
Dyn. viscosity $\mu_F(\frac{\text{kg}}{\text{ms}})$	3.5×10^{-3} [44]	3.5×10^{-3}
Young's modulus $E(\text{Pa})$	$10^5 - 10^6$ [44, 1, 3]	1.0587×10^6
Wall thickness $h(\text{m})$	$1 - 2 \times 10^{-3}$ [44]	0.0009
Wall density $\rho_W(\text{kg/m}^3)$	1.1×10^3 [44]	1.1×10^3
Fluid density $\rho_F(\text{kg/m}^3)$	1050 [44]	1000
Wall viscosity coef. $hC_v/R(\text{Pa}\cdot\text{s})$	$10^3 - 8 \times 10^3$ [1, 2, 3]	0

and plug this into the Navier–Stokes equations (3.1)–(3.3). We look for a solution to the zeroth-order approximation of the problem plus its ϵ-correction. The zeroth-order approximation corresponds to the leading-order approximation of the flow in the limit in which the wavelength of the disturbance and the length scale of tube variation are large compared with the tube radius.

4.1. The zeroth-order approximation. The leading-order Navier–Stokes equations read

$$(4.6) \qquad Sh_0\frac{\partial \tilde{v}_z^0}{\partial \tilde{t}} + (\tilde{v}^0\nabla_{\tilde{r},y})\tilde{v}_z^0 + \frac{\partial \tilde{p}^0}{\partial \tilde{z}} + \frac{\partial \tilde{p}^1}{\partial y} - \frac{1}{Re_0}\left\{\frac{1}{\tilde{r}}\frac{\partial}{\partial \tilde{r}}\left(\tilde{r}\frac{\partial \tilde{v}_z^0}{\partial \tilde{r}}\right) + \frac{\partial^2 \tilde{v}_z^0}{\partial y^2}\right\} = 0,$$

$$(4.7) \qquad Sh_0\frac{\partial \tilde{v}_r^0}{\partial \tilde{t}} + (\tilde{v}^0\nabla_{\tilde{r},y})\tilde{v}_r^0 + \frac{\partial \tilde{p}^0}{\partial r} + \frac{\partial \tilde{p}^1}{\partial \tilde{r}} - \frac{1}{Re_0}\left\{\frac{1}{\tilde{r}}\frac{\partial}{\partial \tilde{r}}\left(\tilde{r}\frac{\partial \tilde{v}_r^0}{\partial \tilde{r}}\right) + \frac{\partial^2 \tilde{v}_r^0}{\partial y^2}\right\} = 0,$$

$$(4.8) \qquad\qquad\qquad \nabla_{\tilde{r},y}\tilde{p}^0 = 0,$$

$$(4.9) \qquad\qquad\qquad \frac{\partial}{\partial \tilde{r}}\left(\tilde{r}\tilde{v}_r^0\right) + \frac{\partial}{\partial y}\left(\tilde{r}\tilde{v}_z^0\right) = 0,$$

$$(4.10) \qquad \text{with } \tilde{v}_r^0, \tilde{v}_z^0, \text{ and } \tilde{p}^1 \text{ 1-periodic in } y \text{ and } \tilde{v}_r^0 = \tilde{v}_z^0 = 0 \text{ at } \tilde{r} = 1 + \frac{\Xi}{R}\tilde{\eta},$$

where $Sh_0 := \frac{\epsilon L\omega^\epsilon}{V}$ and $Re_0 := \frac{\rho_F RV}{\mu_F}$. Here the following scaling for the pressure is used:

$$(4.11) \qquad\qquad p = \frac{\rho_F V^2}{\epsilon}\tilde{p}, \quad \text{thus} \quad C_p = \frac{\rho_F V^2}{\epsilon}.$$

Notice $Sh_0 = \epsilon Sh$ and $Re_0 = Re/\epsilon$. For the average values from Table 4.1 Sh_0 is of order 1 and Re_0 is around 1000. We remark that (4.8) corresponds to the ϵ^{-1}-term and the others to the ϵ^0-term.

The leading-order behavior for the boundary conditions evaluated at the lateral boundary $\tilde{r} = 1 + \frac{\Xi}{R}\tilde{\eta}^0$ is the following:
- The kinematic boundary condition:

$$(4.12) \qquad\qquad\qquad \tilde{v}_r^1 = \frac{\partial \tilde{\eta}^0}{\partial \tilde{t}} + \mathcal{O}(\epsilon^2).$$

- The dynamic boundary condition:

$$(4.13) \qquad \begin{aligned} \tilde{p}^0 - \tilde{p}_{\text{ref}} &= \frac{\epsilon}{\rho_F V^2}\frac{\Xi}{R}\frac{hE}{R(1-\sigma^2)}\left(1 + \frac{h^2}{12R^2}\right)\tilde{\eta}^0 + \tilde{p}_{\text{ref}}\frac{\Xi}{R}\tilde{\eta}^0 \\ &+ \frac{\epsilon}{\rho_F V^2}\frac{\Xi}{R}\frac{hC_V\omega}{R}\left(1 + \frac{h^2}{12R^2}\right)\frac{\partial \tilde{\eta}^0}{\partial \tilde{t}} + \mathcal{O}(\epsilon^2). \end{aligned}$$

Notice that for the parameter values in Table 4.1, $\omega \approx 100$ and the values of the leading-order coefficients are both of order one: $\frac{\epsilon}{\rho_F V^2} \frac{\Xi}{R} \frac{hE}{R(1-\sigma^2)} (1 + \frac{h^2}{12R^2}) = \mathcal{O}(1)$, $\frac{\epsilon}{\rho_F V^2} \frac{\Xi}{R} \frac{hC_V \omega}{R} (1 + \frac{h^2}{12R^2}) = \mathcal{O}(1)$. This is the ϵ^2-approximation of the pressure-displacement relationship describing the linearly viscoelastic cylindrical Koiter shell model. The terms multiplying h^3 account for the bending rigidity of the Koiter shell. These terms are not present in the pressure-displacement relationship describing a viscoelastic membrane.

To obtain a closed system of reduced equations notice that system (4.6)–(4.10) admits a unique strong (nonstationary) unidirectional solution independent of y [48] for every given smooth pressure $\tilde{p}^0$:

$$\text{(4.14)} \qquad \tilde{v}_r^0 = 0, \quad \tilde{v}_z^0 = \tilde{v}_z^0(\tilde{r}, \tilde{z}, \tilde{t}),$$

where $\tilde{v}_z^0$ satisfies

$$\text{(4.15)} \quad \begin{cases} Sh_0 \dfrac{\partial \tilde{v}_z^0}{\partial \tilde{t}} - \dfrac{1}{Re_0} \dfrac{1}{\tilde{r}} \dfrac{\partial}{\partial \tilde{r}} \left(\tilde{r} \dfrac{\partial \tilde{v}_z^0}{\partial \tilde{r}} \right) = -\dfrac{\partial \tilde{p}^0}{\partial \tilde{z}}(\tilde{z}, \tilde{t}), \\[2mm] \tilde{v}_z^0(0, \tilde{z}, \tilde{t}) \text{ bounded}, \quad \tilde{v}_z^0(1 + \Xi\tilde{\eta}^0(\tilde{z}, \tilde{t})/R, \tilde{z}, \tilde{t}) = 0, \quad \text{and } \tilde{v}_z^0(\tilde{r}, \tilde{z}, 0) = 0, \end{cases}$$

and $\tilde{p}^1$ is a linear function of y, independent of $\tilde{r}$. Since $\tilde{p}^1$ is 1-periodic $\tilde{p}^1$ cannot depend on y. Thus, the derivatives of $\tilde{p}^1$ with respect to $\tilde{r}$ and y are both zero.

To complement (4.15) in the calculation of $\tilde{v}_z^0$ and $\tilde{p}^0$ we use the conservation of mass equation (3.3) averaged with respect to the cross-section. The leading-order terms in (3.3) read

$$\frac{\partial}{\partial \tilde{r}} \left(\tilde{r} \tilde{v}_r^1 \right) + \frac{\partial}{\partial \tilde{z}} \left(\tilde{r} \tilde{v}_z^0 \right) = 0.$$

Integrated with respect to $\tilde{r}$ from 0 to $1 + \frac{\Xi}{R}\tilde{\eta}^0$ one obtains

$$\text{(4.16)} \qquad \frac{\partial \left(1 + \frac{\Xi}{R}\tilde{\eta}^0 \right)^2}{\partial \tilde{t}} + \frac{\Xi}{R} \frac{\partial}{\partial \tilde{z}} \int_0^{1 + \frac{\Xi}{R}\tilde{\eta}^0} 2\tilde{v}_z^0 \tilde{r} d\tilde{r} = 0,$$

where we have used the kinematic boundary condition (4.12) to couple the flow velocity and lateral boundary motion.

Equations (4.16), (4.15), and (4.13) give rise to a nonlinear free-boundary problem for the zeroth-order approximation of the flow. In dimensional variables, the nonlinear free-boundary problem for $(\boldsymbol{v}^0, \eta^0, p^0) = (v_z^0, 0, \eta^0, p^0)$ reads

$$\text{(4.17)} \quad \begin{aligned} & \frac{\partial(R+\eta^0)^2}{\partial t} + \frac{\partial}{\partial z} \int_0^{R+\eta^0} 2r v_z^0 dr = 0, \\[2mm] & \varrho_F \frac{\partial v_z^0}{\partial t} - \mu_F \frac{1}{r} \frac{\partial}{\partial r} \left(r \frac{\partial v_z^0}{\partial r} \right) = -\frac{\partial p^0}{\partial z}, \\[2mm] & p^0 - p_{\text{ref}} = \frac{hE}{R^2(1-\sigma^2)} \left(1 + \frac{h^2}{12R^2} \right) \eta^0 + p_{\text{ref}} \frac{\eta^0}{R} + \frac{hC_V}{R^2} \left(1 + \frac{h^2}{12R^2} \right) \frac{\partial \eta^0}{\partial t}, \\[2mm] & v_z^0|_{r=0} - \text{ bounded}, \quad v_z^0|_{r=R+\eta^0} = 0, \quad v_z^0|_{t=0} = 0, \\[2mm] & \eta^0|_{t=0} = 0, \quad p^0|_{z=0} = P_0, \quad p^0|_{z=L} = P_L. \end{aligned}$$

4.2. The first-order correction. The first-order correction to the solution defined by (4.17) is obtained by solving the equations that result from the coefficients at the ϵ^1-terms in the expanded Navier–Stokes equations (3.1)–(3.3)

(4.18)
$$Sh_0 \frac{\partial \tilde{v}_z^1}{\partial \tilde{t}} + \tilde{v}_z^0 \left\{ \frac{\partial \tilde{v}_z^1}{\partial y} + \frac{\partial \tilde{v}_z^0}{\partial \tilde{z}} \right\} + \tilde{v}_r^1 \frac{\partial \tilde{v}_z^0}{\partial \tilde{r}} + \frac{\partial \tilde{p}^1}{\partial \tilde{z}} + \frac{\partial \tilde{p}^2}{\partial y} = \frac{1}{Re_0} \left\{ \frac{1}{\tilde{r}} \frac{\partial}{\partial \tilde{r}} \left(\tilde{r} \frac{\partial \tilde{v}_z^1}{\partial \tilde{r}} \right) + \frac{\partial^2 \tilde{v}_z^1}{\partial y^2} \right\},$$

(4.19)
$$Sh_0 \frac{\partial \tilde{v}_r^1}{\partial \tilde{t}} + \tilde{v}_z^0 \frac{\partial \tilde{v}_r^1}{\partial y} + \frac{\partial \tilde{p}^2}{\partial \tilde{r}} = \frac{1}{Re_0} \left\{ \frac{1}{\tilde{r}} \frac{\partial}{\partial \tilde{r}} \left(\tilde{r} \frac{\partial \tilde{v}_r^1}{\partial \tilde{r}} \right) + \frac{\partial^2 \tilde{v}_r^1}{\partial y^2} \right\},$$

(4.20)
$$\frac{\partial}{\partial \tilde{r}} \left(\tilde{r} \tilde{v}_r^1 \right) + \frac{\partial}{\partial y} \left(\tilde{r} \tilde{v}_z^1 \right) + \tilde{r} \frac{\partial \tilde{v}_z^0}{\partial \tilde{z}} = 0,$$

(4.21)
$$\tilde{v}_r^1, \tilde{v}_z^1, \tilde{p}^2 \text{ 1-periodic in } y; \; \tilde{v}_r^1 = \frac{\partial \tilde{\eta}^0}{\partial \tilde{t}}, \quad \tilde{v}_z^0 = 0 \;\text{ at }\; \tilde{r} = 1 + \frac{\Xi}{R} \tilde{\eta}^0.$$

Using the same arguments as in [9] one can show that $\tilde{p}^1 = \tilde{p}^2 = 0$ and we have a closed linear system, known as a nonstationary Oseen system, defined on a fixed domain $(0, L) \times (0, 1 + \Xi/R\eta^0)$.

To calculate the ϵ-correction to the velocity we look for a solution $\tilde{v}_z^1$ that is independent of the "artificial" fast variable y. In this case the conservation of mass equation (4.20) can be integrated with respect to $\tilde{r}$ to obtain an explicit formula for $\tilde{v}_r^1$ in terms of the already calculated $\tilde{v}_z^0$:

(4.22)
$$\tilde{r} \tilde{v}_r^1 (\tilde{r}, \tilde{z}, \tilde{t}) = \left(1 + \frac{\Xi \tilde{\eta}^0}{R} \right) \frac{\partial \tilde{\eta}^0}{\partial \tilde{t}} + \int_{\tilde{r}}^{1+\Xi\tilde{\eta}^0/R} \frac{\partial \tilde{v}_z^0}{\partial \tilde{z}} (\xi, \tilde{z}, \tilde{t}) \, \xi \, d\xi.$$

The axial momentum equation (4.18) defines a linear problem for $\tilde{v}_z^1$:

(4.23)
$$Sh_0 \frac{\partial \tilde{v}_z^1}{\partial \tilde{t}} - \frac{1}{Re_0} \frac{1}{\tilde{r}} \frac{\partial}{\partial \tilde{r}} \left(\tilde{r} \frac{\partial \tilde{v}_z^1}{\partial \tilde{r}} \right) = -\tilde{v}_r^1 \frac{\partial \tilde{v}_z^0}{\partial \tilde{r}} - \frac{\partial}{\partial \tilde{z}} \left(\frac{(\tilde{v}_z^0)^2}{2} \right),$$

(4.24)
$$\tilde{v}_z^1 (0, \tilde{z}, \tilde{t}) \text{ bounded}, \quad \tilde{v}_z^1 (1 + \Xi \tilde{\eta}^0(\tilde{z}, \tilde{t})/R, \tilde{z}, \tilde{t}) = 0,$$

(4.25)
$$\tilde{v}_z^1 (\tilde{r}, \tilde{z}, 0) = 0, \quad \tilde{v}_z^1 (\tilde{r}, 0, t) = \tilde{v}_z^1 (\tilde{r}, L, t) = 0.$$

Notice that the quadratic transport terms appear in this higher-order approximationi. They are linearized around the zeroth-order approximation of the solution.

Equations (4.22)–(4.25) define the ϵ-correction of the solution. In dimensional form the system reads

(4.26)
$$v_r^1 (r, z, t) = \frac{1}{r} \left(R \frac{\partial \eta^0}{\partial t} + \int_r^R \xi \frac{\partial v_z^0}{\partial z} (\xi, z, t) d\xi \right),$$
$$\rho_F \frac{\partial v_z^1}{\partial t} - \mu_F \frac{1}{r} \frac{\partial}{\partial r} \left(r \frac{\partial v_z^1}{\partial r} \right) = -\rho_F \left(v_r^1 \frac{\partial v_z^0}{\partial r} + v_z^0 \frac{\partial v_z^0}{\partial z} \right),$$
$$v_z^1|_{\tilde{r}=0} - \text{ bounded}, \quad v_z^1|_{r=R} = 0, \quad v_z^1|_{t=0} = 0.$$

PROPOSITION 4.1. *The velocity field $\boldsymbol{v} = (v_z^0 + v_z^1, v_r^1)$, the radial displacement $\eta = \eta^0$, and the pressure $p = p^0$, defined by (4.17) and (4.26), satisfy the original problem (3.1)–(3.10) to $\mathcal{O}(\epsilon^2)$.*

The proof is the same as that of Proposition 7.1 in [9].

We end this section by summarizing the main assumptions under which the simplified, effective problem (4.17), (4.26) holds and the parameter values assumed.

Assumptions.

(1) The domain is cylindrical with small aspect ratio $\epsilon = R_{\max}/L$.
(2) The problem is axially symmetric.
(3) Longitudinal displacement is negligible.
(4) Radial displacement is not too large, i.e., $\delta := \Xi/R \leq \epsilon$.
(5) The reference tube radius varies slowly: $R'(z) < \epsilon$.
(6) The Reynolds number Re is small to medium (Re ≈ 1000).
(7) The z-derivatives of the nondimensional quantities are $O(1)$ (not too large).

5. Viscoelasticity of the fluid-structure interaction. We emphasize in this section that the viscoelastic behavior of the coupled fluid-structure interaction problem comes from two distinct effects. One is the viscoelasticity of the structure itself, and the other is the viscoelasticity due to the interaction between the structure (not necessarily viscoelastic) with a viscous fluid. To explicitly capture the leading-order effects that the viscous fluid imparts on the motion of the structure we proceed as follows. First, we simplify the free-boundary problem (4.17) by expanding the underlying problem (4.17), (4.26), with respect to the radial displacement. The free-boundary problem will be approximated by two fixed boundary problems of similar form. Each of the two fixed boundary problems consists of solving a system of two equations (see (5.1), (5.3)) that are of hyperbolic-parabolic type. In each of the two problems, we can "explicitly solve" the parabolic equation for the velocity, plug the velocity into the resulting equation for the structure, and obtain a single equation describing the motion of the structure. The resulting equation incorporates the viscous fluid effects in terms of a convolution integral. If we will assume, for the moment, that the structure is purely elastic, the resulting equation describes the dynamics of an elastic structure under a viscous fluid load; see (5.11). It corresponds to a model of a viscoelastic string with viscous long-term memory effects. Thus, the fluid viscosity influences the dynamics of an elastic structure through a long-term memory effect.

We begin by expanding the free-boundary problem (4.17) and the ϵ-correction (4.26) with respect to the radial displacement whose magnitude is measured, in nondimensional variables, by Ξ/R. Thus, assume that

$$\delta := \frac{\Xi}{R} \leq \epsilon$$

and introduce the following expansions with respect to δ:

$$\tilde{\eta}^0 = \tilde{\eta}^{0,0} + \delta\tilde{\eta}^{0,1} + \cdots, \quad \tilde{p}^0 = \tilde{p}^{0,0} + \delta\tilde{p}^{0,1} + \cdots,$$
$$v_z^0 = v_z^{0,0} + \delta v_z^{0,1} + \cdots, \quad \tilde{v}_z^1 = \tilde{v}_z^{1,0} + \cdots, \quad \tilde{v}_r^1 = \tilde{v}_r^{1,0} + \cdots.$$

The first superscript denotes the expansion with respect to ϵ and the second with respect to δ. Then using the same approach as in [9] one obtains a set of equations approximating the original problem to the ϵ^2-accuracy. The resulting problem, in dimensional variables, consists of finding the functions

$$v_z = v_z^{0,0} + v_z^{0,1} + v^{1,0} + \mathcal{O}(\epsilon^2), \ v_r = v_r^{1,0} + \mathcal{O}(\epsilon^2), \ \eta = \eta^{0,0} + \mathcal{O}(\epsilon^2) \, p = p^{0,0} + \mathcal{O}(\epsilon^2)$$

satisfying the following set of closed, well-defined problems.

The zeroth-order approximation. Find $(\eta^{0,0}, v_z^{0,0})$ such that

(5.1)
$$\frac{\partial \eta^{0,0}}{\partial t} + \frac{1}{R}\frac{\partial}{\partial z}\int_0^R rv_z^{0,0}dr = 0,$$
$$\varrho_F\frac{\partial v_z^{0,0}}{\partial t} - \mu_F\frac{1}{r}\frac{\partial}{\partial r}\left(r\frac{\partial v_z^{0,0}}{\partial r}\right) = -\frac{\partial p^{0,0}}{\partial z},$$
$$v_z^{0,0}|_{r=0} - \text{ bounded}, \quad v_z^{0,0}|_{t=R} = 0, \quad v_z^{0,0}|_{t=0} = 0,$$
$$\eta^{0,0}|_{t=0} = 0, \quad p^{0,0}|_{z=0} = P_0, \quad p^{0,0}|_{z=L} = P_L,$$

where

(5.2) $$p^{0,0} = \frac{Eh}{(1-\sigma^2)R}\left(1 + \frac{h^2}{12R^2}\right)\frac{\eta^{0,0}}{R} + p_{\text{ref}}\frac{\eta^{0,0}}{R} + \frac{hC_v}{R^2}\left(1 + \frac{h^2}{12R^2}\right)\frac{\partial \eta^{0,0}}{\partial t}.$$

The δ correction. Find $(\eta^{0,1}, v_z^{0,1})$ such that

(5.3)
$$\frac{\partial \eta^{0,1}}{\partial t} + \frac{1}{R}\frac{\partial}{\partial z}\int_0^R rv_z^{0,1}dr = -\frac{1}{2R}\frac{\partial}{\partial t}\left(\eta^{0,0}\right)^2,$$
$$\varrho_F\frac{\partial v_z^{0,1}}{\partial t} - \mu_F\frac{1}{r}\frac{\partial}{\partial r}\left(r\frac{\partial v_z^{0,1}}{\partial r}\right) = -\frac{\partial p^{0,1}}{\partial z},$$

$$v_z^{0,1}|_{r=0} - \text{ bounded}, \quad v_z^{0,1}|_{r=R} = -\eta^{0,0}\frac{\partial v_z^{0,0}}{\partial r}|_{r=R}, \quad v_z^{0,1}|_{t=0} = 0,$$
$$\eta^{0,1}|_{t=0} = 0, \quad \eta^{0,1}|_{z=0} = 0, \quad \eta^{0,1}|_{z=L} = 0,$$

where

(5.4)
$$p^{0,1} = \left(\frac{Eh}{(1-\sigma^2)R}\left(1 + \frac{h^2}{12R^2}\right) + p_{\text{ref}}\right)\left(\frac{\eta^{0,1}}{R} - \left(\frac{\eta^{0,0}}{R}\right)^2\right)$$
$$+ \frac{hC_v}{R^2}\left(1 + \frac{h^2}{12R^2}\right)\left(\frac{\partial \eta^{0,1}}{\partial t} - \frac{\eta^{0,0}}{R}\frac{\partial \eta^{0,1}}{\partial t}\right).$$

The ϵ-correction. Find $(v_r^{1,0}, v_z^{1,0})$ such that

(5.5) $$v_r^{1,0}(r,z,t) = \frac{1}{r}\left(R\frac{\partial \eta^{0,0}}{\partial t} + \int_r^R \xi\frac{\partial v_z^{0,0}}{\partial z}(\xi,z,t)d\xi\right),$$

(5.6) $$\rho_F\frac{\partial v_z^{1,0}}{\partial t} - \mu_F\frac{1}{r}\frac{\partial}{\partial r}\left(r\frac{\partial v_z^{1,0}}{\partial r}\right) = -\rho_F\left(v_r^{1,0}\frac{\partial v_z^{0,0}}{\partial r} + v_z^{0,0}\frac{\partial v_z^{0,0}}{\partial z}\right),$$
$$v_z^{1,0}|_{\bar{r}=0} - \text{ bounded}, \quad v_z^{1,0}|_{r=R} = 0, \quad v_z^{1,0}|_{t=0} = 0.$$

Systems (5.1) and (5.3) can be solved by considering the auxiliary problem

(5.7) $$\begin{cases} \dfrac{\partial \zeta}{\partial t} - \dfrac{1}{r}\dfrac{\partial}{\partial r}\left(r\dfrac{\partial \zeta}{\partial r}\right) = 0 & \text{in } (0,R) \times (0,\infty), \\ \zeta(0,t) \text{ is bounded}, \quad \zeta(R,t) = 0 \text{ and } \zeta(r,0) = 1. \end{cases}$$

For example, the solution of the parabolic equation for the velocity $v_z^{0,0}$ can be written as the convolution

$$v_z^{0,0} = -\frac{1}{\rho_F}\int_0^t \zeta\left(r, \frac{\mu_F(t-\tau)}{\rho_F}\right)\frac{\partial p^{0,0}}{\partial z}(z,\tau)d\tau.$$

Plugging this expression for the velocity into the first equation one obtains

$$(5.8) \qquad \frac{\partial \eta^{0,0}}{\partial t} - \frac{1}{\rho_F R} \frac{\partial}{\partial z} \int_0^R r \int_0^t \zeta \left(r, \frac{\mu_F(t-\tau)}{\rho_F} \right) \frac{\partial p^{0,0}}{\partial z}(z,\tau) d\tau dr = 0.$$

Denote the mean of ζ in the radial direction by

$$(5.9) \qquad \mathcal{K}(t) = 2 \int_0^R \zeta(r,t) \, r dr,$$

and assume, for the moment, that the Koiter shell is purely elastic so that

$$p^{0,0} = C_0 \eta^{0,0}, \text{ where } C_0 = \frac{h}{R^2} \frac{E}{1-\sigma^2} \left(1 + \frac{h^2}{12R^2} \right) + \frac{p_{\text{ref}}}{R}.$$

Then (5.8) becomes

$$(5.10) \qquad \frac{\partial \eta^{0,0}}{\partial t} - \frac{C_0}{2\rho_F R} \int_0^t \mathcal{K} \left(\frac{\mu_F(t-\tau)}{\rho_F} \right) \frac{\partial^2 \eta^{0,0}}{\partial z^2} d\tau = 0.$$

Differentiate with respect to t to obtain

$$(5.11) \qquad \frac{\partial^2 \eta^{0,0}}{\partial t^2} = \frac{C_0 R}{2\rho_F} \frac{\partial^2 \eta^{0,0}}{\partial z^2} + \mu_F \frac{C_0}{2\rho_F^2 R} \int_0^t \mathcal{K}' \left(\frac{\mu_F(t-\tau)}{\rho_F} \right) \frac{\partial^2 \eta^{0,0}}{\partial z^2}.$$
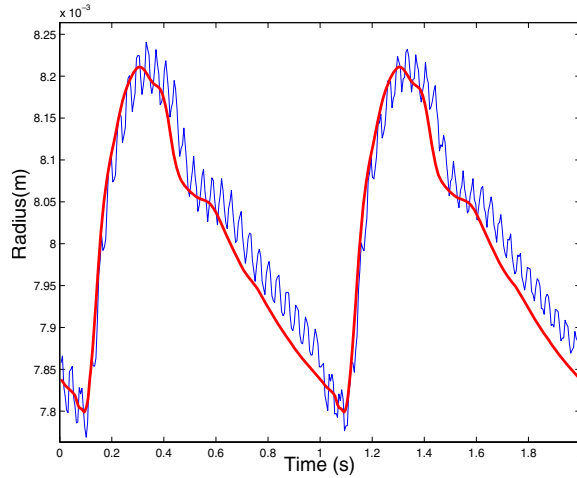

FIG. 5.1. *A comparison between the solutions of* (5.11) *with* $\mu_F = 0$ *(thin solid line) and* $\mu_F = 3.5 \times 10^{-3}$ *(thick solid line). The radius, shown in these graphs, is taken at the midpoint of the tube during two cardiac cycles.*

This is a model describing the motion of a linearly viscoelastic string with the viscous effects described by the convolution integral on the right-hand side of (5.11). The kernel in the convolution corresponds to the derivative of $\mathcal{K}$ which decays in time exponentially fast, with the decay rate equal to the first zero of the Bessel function J_0. This is the only term that incorporates the viscosity of the fluid μ_F. Thus, the fluid impacts the motion of the structure through this long-term memory effect. Numerical simulations presented in Figure 5.1 show the motion of the structure (displacement $\eta^{0,0}$) with $\mu_F = 0$ and with $\mu_F = 3.5 \times 10^{-3}$. The smoothing by the viscous fluid dissipation is obvious.
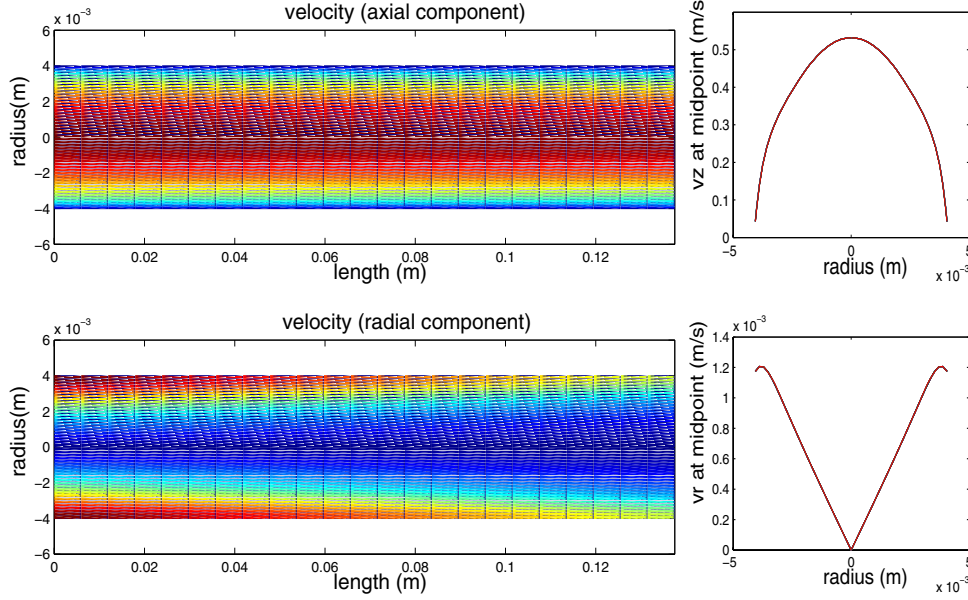
FIG. 6.1. *The axial (top) and radial (bottom) components of the velocity obtained at a first half of the systole (1/6 of the cardiac cycle). The magnitude of the axial component of the velocity is between 0 and 0.52 m/s. The magnitude of the radial component of the velocity is between 0 and 0.0014 m/s. The pictures on the right show the velocity profiles calculated at the midpoint of the tube.*

6. Numerical algorithm. To solve problems (5.1) and (5.3) numerically it is convenient to rewrite each of the systems of equations as a second-order hyperbolic-parabolic problem. Namely, after differentiating the first equation in (5.1) with respect to time, and plugging the second equation into the first, problem (5.1) can be rewritten as

$$(6.1) \qquad \frac{\partial^2 \eta^{0,0}}{\partial t^2} - \frac{R}{2\rho_F} \frac{\partial^2 p^{0,0}}{\partial z^2} = -\frac{\mu_F}{\rho_F} \frac{\partial}{\partial z} \left(\left. \frac{\partial v_z^{0,0}}{\partial r} \right|_{r=R} \right),$$

$$(6.2) \qquad \rho_F \frac{\partial v_z^{0,0}}{\partial t} - \mu_F \frac{1}{r} \frac{\partial}{\partial r} \left(r \frac{\partial v_z^{0,0}}{\partial r} \right) = -\frac{\partial p^{0,0}}{\partial z},$$

with the initial and boundary conditions specified in (5.1) and $p^{0,0}$ substituted by (5.2). Similarly, problem (5.3) can be written as

$$(6.3) \qquad \frac{\partial^2 \eta^{0,1}}{\partial t^2} - \frac{R}{2\rho_F} \frac{\partial^2 p^{0,1}}{\partial z^2} = -\frac{\mu_F}{\rho_F} \frac{\partial}{\partial z} \left(\left. \frac{\partial v_z^{0,0}}{\partial r} \right|_{r=R} \right) - \frac{1}{2R} \frac{\partial^2}{\partial t^2} \left(\eta^{0,0} \right)^2,$$

$$(6.4) \qquad \rho_F \frac{\partial v_z^{0,1}}{\partial t} - \mu_F \frac{1}{r} \frac{\partial}{\partial r} \left(r \frac{\partial v_z^{0,1}}{\partial r} \right) = -\frac{\partial p^{0,1}}{\partial z},$$

with initial and boundary conditions given in (5.3) and $p^{0,1}$ substituted by (5.4). The first equation in both subproblems can be thought off as a one-dimensional wave equation in z and t, and the second as the one-dimensional heat equation in r and t. The systems for the $0,0$ and $0,1$ approximations have the same form. They are solved using a one-dimensional finite element method. Since the mass and stiffness matrices are the same for both problems, up to the boundary conditions, they are

generated only once. Both systems are solved simultaneously using a time-iteration procedure. First, the parabolic equation is solved for $v_z^{0,0}$ at the time step t_{i+1} by explicitly evaluating the right-hand side at the time-step t_i. Then the wave equation is solved for $\eta^{0,0}$ with the evaluation of the right-hand side at the time-step t_{i+1}. Using these results for $v_z^{0,0}$ and $\eta^{0,0}$, computed at t_{i+1}, a correction at t_{i+1} is calculated by repeating the process with the updated values of the right-hand sides. This method is a version of the Douglas–Rachford time-splitting algorithm which is known to be of first-order accuracy.

Calculating approximation $1, 0$ is straightforward once the approximations $0, 0$ and $0, 1$ are obtained. In this algorithm a sequence of one-dimensional problems is solved, so the numerical complexity is that of one-dimensional solvers. However, leading-order two-dimensional effects are captured to the ϵ^2-accuracy. Figure 6.1 presents the axial and radial components of the velocity, showing two-dimensional effects that cannot be captured using one-dimensional models.

7. Experimental validation. A mock circulatory loop was used to validate our simplified, effective mathematical flow model (5.1)–(5.6). The circulatory loop was assembled at the Research Laboratory at the Texas Heart Institute. Figure 7.1 shows the experimental setup and a sketch of the main components of the mock circulatory loop. The main components of the flow loop include the left ventricular assist device (LVAD Heart Mate, Thoratex Corp., Woburn, MA), which is a pulsatile flow pump used in patients with failing hearts to aid the function of the left ventricle, the inlet and outlet LVAD valves, two compliance chambers (wash bottles; 250 ml in volume), a reservoir (Nalgene canister), and pressure transducers (TruEave, Edwards Lifesciences, Irvine, CA) placed at the inlet and outlet of the test segment. Latex tubing (Kent Elastomer Products Inc.) was used to simulate compliant vessels. See Figure 7.1. The straight latex tube segment was attached to the hard plastic connectors placed at the inlet and at the outlet of the segment, keeping the inlet and outlet displacement together with its derivative equal to zero, i.e., $\eta = \partial\eta/\partial z = 0$ at $z = 0, L$, as well as the inlet and outlet velocity approximately such that $v_r = 0$.
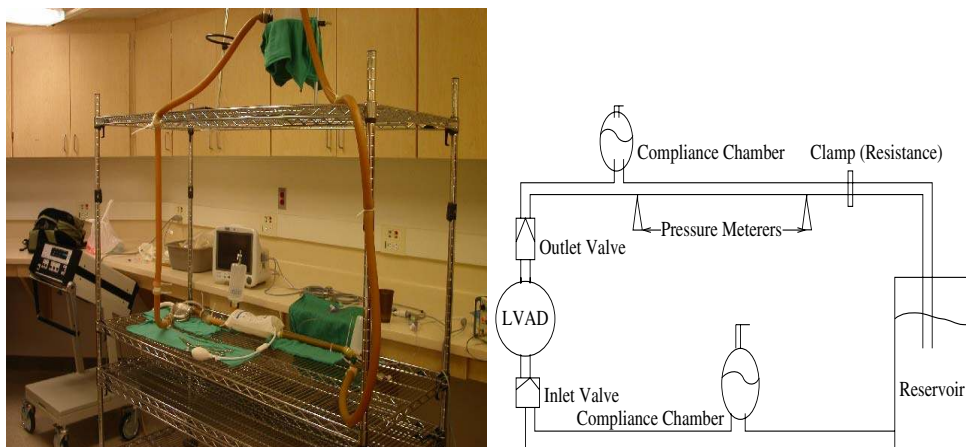

FIG. 7.1. *Flow loop at the Research Laboratory at the Texas Heart Institute (left), a sketch of the flow loop (right).*

One of the goals of this experiment was to recreate the pressure waves and fluid velocity at the middle section of the straight test segment similar to those typical

for the human abdominal aorta. To achieve this goal a clamp located downstream from the test segment was added to mimic downstream resistance by the capillary bed. Figure 7.2(left) shows the measured (filtered) pressure data at the inlet and at the outlet of the test segment. This compares well with the typical inlet and outlet pressure data of the human abdominal aorta, shown in Figure 7.2(right). Ultrasonic imaging and Doppler methods were used to measure the axial velocity of the flow. Nondairy coffee creamer was dispersed in water to enable reflection for ultrasound measurements. A high-frequency (20 MHz) single crystal probe was inserted through a catheter at several locations of the tube. This method has been validated in vivo by measuring the velocity and wall motion in mice to a precision of 0.1 um; see [25, 26].
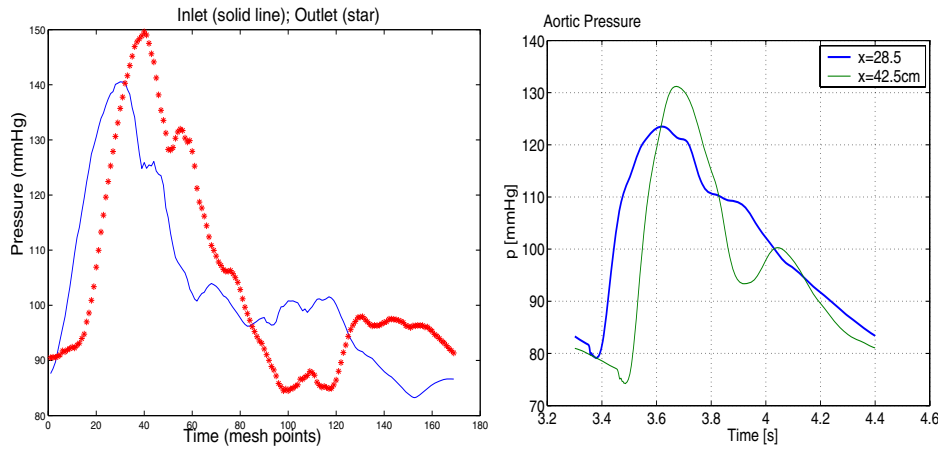

FIG. 7.2. *Inlet and outlet pressure data used in the numerical simulations. Left: Circulatory flow loop data (filtered). Right: aortic data* [14].
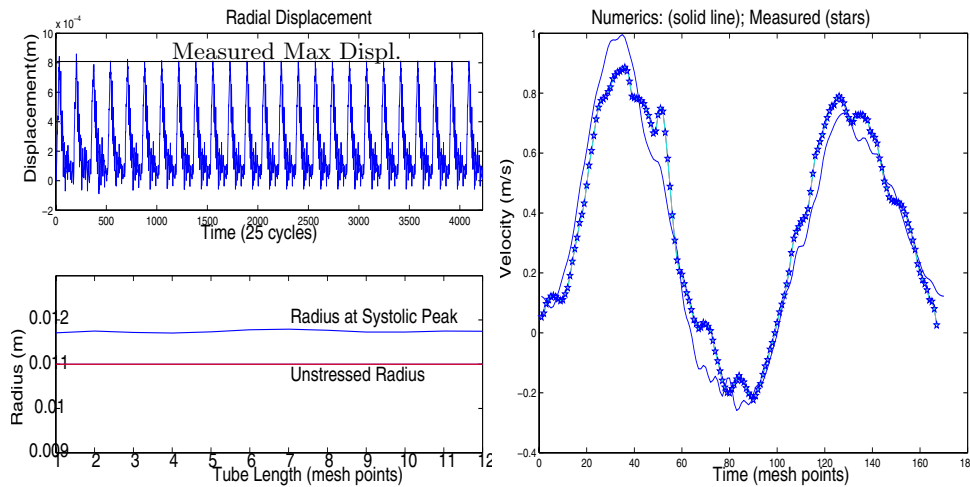

FIG. 7.3. *The figure shows a comparison between the numerical simulations and the experimental measurements. Left: Displacement. Right: axial component of the velocity, evaluated at the midpoint of the tube (midpoint with respect to the length and the diameter of the tube). The solid line corresponds to the numerically calculated solution; the line with asterisks corresponds to the experimentally collected data.*

To determine Young's modulus of the tube wall we measured the tube diameter d at the reference pressure of 84 mmHg ($d = 2.22$ cm) and at the maximal systolic pressure of 148 mmHg ($d = 2.38$ cm), utilizing the linear pressure-displacement relationship described by the equations of p^0 in (4.17) with $C_V = 0$ and the data for the tube wall thickness provided by the manufacturer of the latex tube, Kent Elastomer Products Inc. The value of $E = 1.0587 \times 10^6$ Pa was obtained. Using the numerical solver described in section 6 system of equations (5.1)–(5.6) was solved. The results were compared with the experimental measurements. At the top of Figure 7.3(left) is a comparison between the numerically calculated displacement and the experimentally measured maximal displacement of 0.0008 m. Figure 7.3(right) shows a comparison between the numerically calculated (solid line) and experimentally measured (asterisks) axial velocity. Excellent agreement was obtained indicating that this model captures well the fluid-structure interaction between a linearly elastic structure such as a latex tube, and the flow of a viscous incompressible fluid such as water, in the flow regime corresponding to the abdominal aorta.

8. Hysteresis behavior of viscoelastic arteries. In this section we compare the results of our viscoelastic model with the measurement of the viscoelastic properties of the human and canine arteries presented in [1, 2, 3]. In [1] Armentano et al. studied the viscoelastic aortic properties in dogs. In particular, they measured the magnitude of the viscous modulus corresponding to our coefficient hC_v/R. The values corresponding to dogs aortas, reported in [1], belong to the interval

$$\frac{hC_v}{R}\Big|_{\text{(dog aorta)}} \in (3.8 \pm 1.3 \times 10^4, 7.8 \pm 1.1 \times 10^4) \, dyn \cdot \text{s/cm}^2$$
$$= (3.8 \pm 1.3 \times 10^3, 7.8 \pm 1.1 \times 10^3) \, \text{Pa} \cdot \text{s}.$$

Taking into account the radius of the studied aortas (≈ 0.008 m) and the average wall thickness (≈ 0.0014 m), one obtains

$$C_v|_{\text{(dog aorta)}} \in (2.17 \times 10^4, 4.45 \times 10^4) \, \text{Pa} \cdot \text{s}.$$

In [1] the measurements of the viscoelastic properties of the canine aorta were obtained, showing a hysteresis in the stress-strain diagram, where the stress (τ) and strain (e) were defined using

(8.1)
$$\tau = \frac{2p(r_e r_i)^2}{r_e^2 - r_i^2} \frac{1}{R^2}, \quad e = \frac{R + \eta}{R}.$$

Here r_e and r_i are the external and internal vessel radii calculated using $r_{e,i} = R \pm 0.5 \, h$. The results of the measurements are shown in Figure 8.1(left). We used the data presented in [1] as a guide in the numerical simulation of the dynamics of the canine aorta utilizing the effective viscoelastic model (4.17), (4.26). Unfortunately, [1] does not include the pressure data at the inlet and outlet of the canine aorta. Thus, it was impossible to recreate the simulation that would correspond exactly to the scenario studied in [1]. However, using the data available to us, in particular the viscous modulus C_V, we were able to approximate the scenario studied in [1] and capture the main viscoelastic properties of the canine aorta. The results are shown in Figure 8.1. The top figures show the pressure and the scaled diameter in one cardiac cycle. Both waves exhibit the same morphology, but the diameter shows a time delay with respect to the pressure, which is due to the viscosity of the vessel wall. The
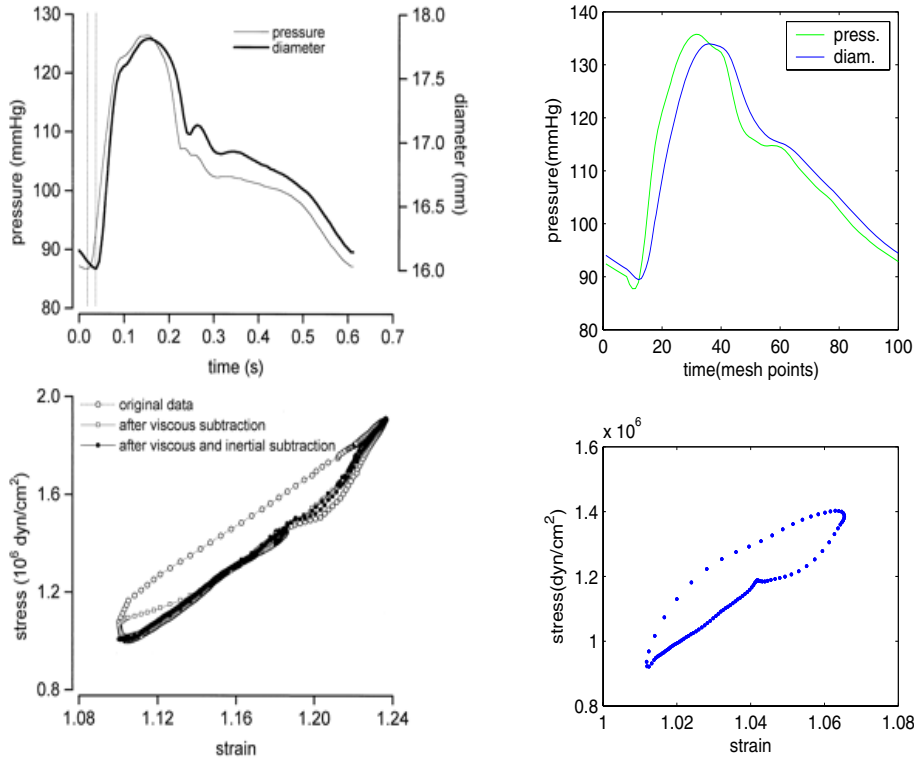
FIG. 8.1. *Left: Measured viscoelastic behavior of the canine aorta reported in* [1] *(top: aortic diameter and pressure wave forms, bottom: stress-strain relationship). Right: Numerical simulation of the reduced one-and-a-half-dimensional model showing viscoelastic behavior of vessel walls (top: aortic diameter and pressure wave forms, bottom: stress-strain relationship).*

bottom figures show the hysteresis behavior in the stress-strain relationship. The upper "half" of the hysteresis corresponds to the loading and the lower "half" to the unloading portion of the cardiac cycle. The hysteresis curves and the time-lag between the pressure and scaled diameter show similar qualitative behavior.

An even better approximation of the hysteresis behavior in the dynamics of major arteries was obtained for the data corresponding to a healthy human femoral artery. One reason for this is that the inlet and outlet pressure data that were used in all of our numerical simulations correspond to the human data. We compared our numerical simulations to the measurements data presented in [2]. In [2] Armentano et al. estimated the magnitude of the coefficient multiplying the term $\partial D/\partial t$, where D is the vessel diameter of a human femoral artery. The value of the coefficient was estimated to be $266 \times$ Pa $\cdot$ s/m. Using the values for the measured femoral artery diameter ($0.00625m$) and the wall thickness (0.001 m), one obtains

$$(8.2) \qquad C_v|_{\text{(human femoral)}} \approx 5.2 \times 10^3 \text{ Pa} \cdot \text{s}.$$

Thus, the corresponding viscous modulus hC_v/R is

$$(8.3) \qquad \left.\frac{hC_v}{R}\right|_{\text{(human femoral)}} \approx 1.6 \times 10^3 \text{ Pa} \cdot \text{s},$$
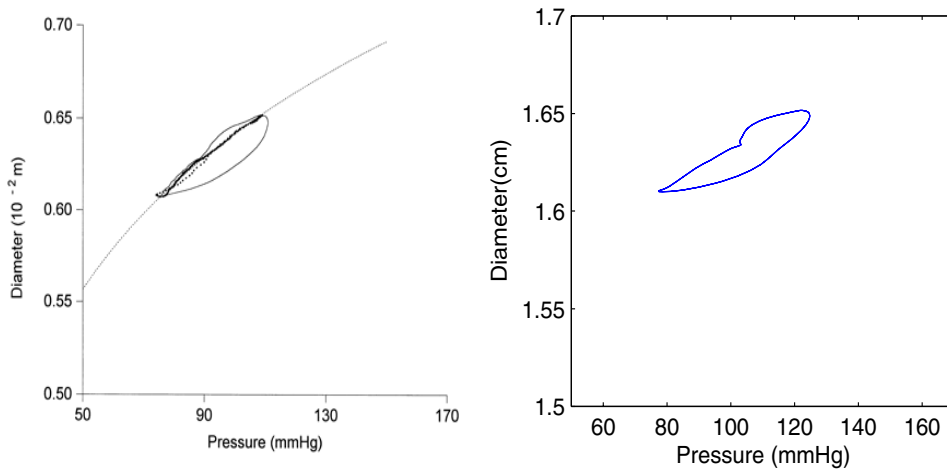
FIG. 8.2. *Left: Measurements of the diameter-pressure hysteresis loop in human femoral artery reported in [2]. Right: Numerical simulation of the diameter-pressure hysteresis loop with parameters from Table 4.1 ($E = 1.3 \times 10^6$ Pa, $h = 0.001$ m, $R = 0.008$ m, $L = 0.13$ m, $hC_v/R = 10^3$ Pa · s).*

which is of the same order of magnitude as the viscous modulus corresponding to the dogs aortas. Figure 8.2 shows a comparison between our numerical simulations and measurements. There, a pressure-diameter relationship is plotted, showing hysteresis behavior. The graph in Figure 8.2(left) corresponds to the measurements of the human femoral artery reported in [2], and the graph in Figure 8.2(right) shows the pressure-diameter relationship in the simulations obtained using the reduced model (5.1), (5.6). Again, similar viscoelastic behavior is detected.
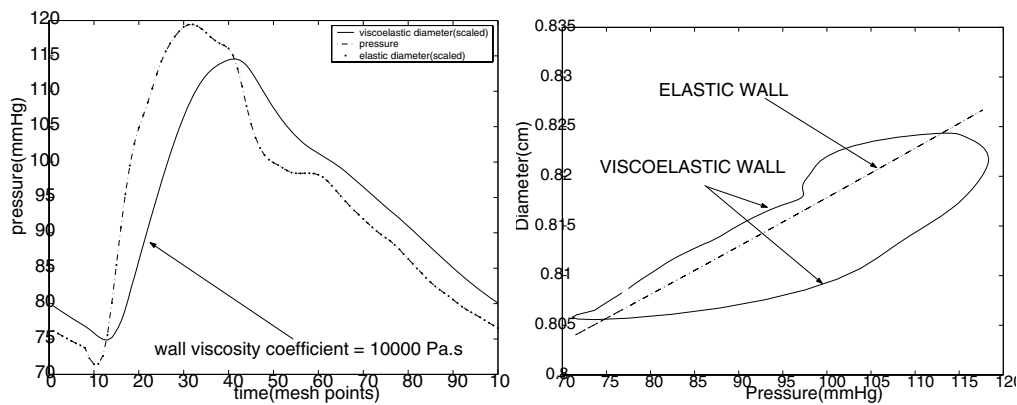

FIG. 9.1. *Elastic vs. viscoelastic wall model. The figure on the left shows the pressure and the scaled diameter (elastic and viscoelastic) over one cardiac cycle (the pressure wave and the elastic diameter coincide). The figure on the right shows the pressure-diameter plot for the viscoelastic model (hysteresis) and the elastic model (straight line).*

9. Elastic vs. viscoelastic model. We conclude this manuscript by presenting a comparison between the results of the fluid-structure interaction models assuming elastic vs. viscoelastic wall model with a relatively large viscoelastic constant $hC_v/R =$

10^4 Pa $\cdot$ s. Figure 9.1(left) shows the pressure and the scaled diameter values for the two models plotted over one cardiac cycle. One can easily detect the time-shift in the diameter of the viscoelastic model compared with the diameter of the elastic wall model which coincides (the scaled diameter) with the pressure wave. Figure 9.1(right) shows the pressure-diameter plot emphasizing the hysteresis in the viscoelastic model superimposed over the straight line pressure-diameter plot corresponding to the elastic model.

10. Conclusions. In this manuscript we derived a simple, effective closed model that describes blood flow through viscoelastic arteries in cylindrical geometry assuming axially symmetric flows. Using homogenization theory and asymptotic analysis, this fluid-structure interaction problem was reduced to a free-boundary problem of hyperbolic-parabolic type in two space dimensions. Although the model is two-dimensional, its simple form allows the use of one-dimensional solvers giving rise to a numerical algorithm of one-dimensional complexity. In contrast with the "classical" one-dimensional models where an ad hoc assumption on the axial velocity profile needs to be used to close the model, the system we obtained in this manuscript is closed, producing the axial as well as radial velocity as a solution of the problem. We showed that the reduced model approximates the original three-dimensional axially symmetric model to the ϵ^2-accuracy, where ϵ is the aspect ratio of the tube approximating straight arterial sections. The main novelty in this manuscript is the derivation of a viscoelastic cylindrical Koiter shell model to describe the behavior of arterial walls. Viscoelasticity of Kelvin–Voigt type was utilized to derive the model which appoximates well the hysteresis behavior observed in the vessel wall measurements. We showed that in this fluid-structure interaction model bending rigidity of arterial walls plays a nonnegligible role in the leading-order approximation of the problem. This effect, together with the viscosity of vessel walls, explicitly derived in this manuscript, provides the regularizing mechanisms for the stability of the solutions.

REFERENCES

[1] R. L. Armentano, J. G. Barra, J. Levenson, A. Simon, and R. H. Pichel, *Arterial wall mechanics in conscious dogs: Assessment of viscous, inertial, and elastic moduli to characterize aortic wall behavior*, Circ. Res., 76 (1995), pp. 468–478.

[2] R. L. Armentano, J. L. Megnien, A. Simon, F. Bellenfant, J. G. Barra, and J. Levenson, *Effects of hypertension on viscoelasticity of carotid and femoral arteries in humans*, Hypertension, 26 (1995), pp. 48–54.

[3] R. D. Bauer, R. Busse, A. Shabert, Y. Summa, and E. Wetterer, *Separate determination of the pulsatile elastic and viscous forces developed in the arterial wall in vivo*, Pflugers Arch., 380 (1979), pp. 221–226.

[4] A. Bensoussan, J.-L. Lions, and G. Papanicolaou, *Asymptotic Analysis for Periodic Structures*, North–Holland, Amsterdam, 1978.

[5] S. Čanić and E.-H. Kim, *Mathematical analysis of the quasilinear effects in a hyperbolic model of blood flow through compliant axi–symmetric vessels*, Math. Methods Appl. Sci., 26 (2003), pp. 1161–1186.

[6] S. Čanić, A. Mikelić, and J. Tambača, *A two-dimensional effective model describing fluid-structure interaction in blood flow: Analysis, simulation and experimental validation*, Comptes Rendus Méchanique Acad. Sci. Paris, 333 (2005), pp. 867–883.

[7] S. Čanić and A. Mikelić, *Effective equations describing the flow of a viscous incompressible fluid through a long elastic tube*, Comptes Rendus Méchanique Acad. Sci. Paris, 330 (2002), pp. 661–666.

[8] S. Čanić and A. Mikelić, *Effective equations modeling the flow of a viscous incompressible fluid through a long elastic tube arising in the study of blood flow through small arteries*, SIAM J. Appl. Dyn. Syst., 2 (2003), pp. 431–463.

[9] S. Čanić, D. Lamponi, A. Mikelić, and J. Tambača, *Self-consistent effective equations modeling blood flow in medium-to-large compliant arteries*, Multiscale Model. Simul., 3 (2005), pp. 559–596.

[10] A. Chambolle, B. Desjardins, M. Esteban, and C. Grandmont, *Existence of weak solutions for an unsteady fluid-plate interaction problem*, J Math. Fluid Mech., 7 (2005), pp. 368–404.

[11] P. G. Ciarlet, *Mathematical Elasticity. Vol.* III. *Theory of Shells*, Stud. Math. Appl. 29, North–Holland, Amsterdam, 2000.

[12] P. G. Ciarlet and V. Lods, *Asymptotic analysis of linearly elastic shells.* III. *Justification of Koiter's shell equations*, Arch. Rational Mech. Anal., 136 (1996), pp. 191–200.

[13] P. G. Ciarlet and V. Lods, *Asymptotic analysis of linearly elastic shells. Generalized membrane shells*, J. Elasticity, 43 (1996), pp. 147–188.

[14] C. Chmielevsky, *A Comparison of Two Models Predicting Blood Flow in the Systemic Arteries*, M.S. thesis, North Carolina State University, Raleigh, NC, 2004.

[15] D. Coutand and S. Shkoller, *Motion of an elastic solid inside of an incompressible viscous fluid*, Arch. Ration. Mech. Anal., 176 (2005), pp. 25–102.

[16] D. Coutand and S. Shkoller, *Interaction between quasilinear elasticity and the Navier-Stokes equations*, Arch. Ration. Mech. Anal., 179 (2006), pp. 303–352.

[17] H. Demiray, *Small but finite amplitude waves in a prestressed viscoelastic thin tube filled with an inviscid fluid*, Internat. J. Engrg. Sci., 35 (1997), pp. 353–363.

[18] S. X. Deng, J. Tomioka, J. C. Debes, and Y. C. Fung, *New experiments on shear modulus of elasticity of arteries*, Am. J. Physiol. Heart Circ. Physiol., 266 (1994), pp. 1–10.

[19] P. Destuynder, *A classification of thin shell theories*, Acta Appl. Math., 4 (1985), pp. 15–63.

[20] A. C. Eringen, *Mechanics of Continua*, Wiley, New York, 1967.

[21] Y. C. Fung, *Biomechanics: Circulation*, 2nd ed., Springer, New York, 1993.

[22] Y. C. Fung, *Biomechanics: Mechanical Properties of Living Tissues*, Springer, New York, 1993.

[23] J. B. Grotberg and O. E. Jensen, *Biofluid mechanics in flexible tubes*, in Annual Review of Fluid Mechanics, Annu. Rev. Fluid Mech. 36, Annual Reviews, Palo Alto, CA, 2004, pp. 121–147.

[24] M. Guidorzi, M. Padula, and P. Plotnikov, *Hopf solutions to a fluid-elastic interaction model*, Math. Models Methods Appl. Sci., submitted.

[25] C. J. Hartley, *Ultrasonic blood flow and velocimetry*, in McDonald's Blood Flow in Arteries, Theoretical, Experimental and Clinical Principles, 4th ed., W. W. Nichols and M. F. O'Rourke, Arnold, London, 1998, pp. 154–169.

[26] C. J. Hartley, G. Taffet, A. Reddy, M. Entman, and L. Michael, *Noninvasive cardiovascular phenotyping in mice*, ILAR J., 43 (2002), pp. 147–158.

[27] M. Heil and T. J. Pedley, *Large axisymmetric deformations of a cylindrical shell conveying a viscous flow*, J. Fluids and Struct., 9 (1995), pp. 237–256.

[28] U. Hornung, ed., *Homogenization and Porous Media*, Interdiscip. Appl. Math. 6, Springer, New York, 1997.

[29] J. D. Humphrey, *Mechanics of the arterial wall: Review and directions*, Crit. Rev. Biomed. Eng., 23 (1995), pp. 1–162.

[30] R. E. Klabunde, *Cardiovascular Physiology Concepts*, http://cvphysiology.com/index.html (2005).

[31] W. T. Koiter, *A consistent first approximation in the general theory of thin elastic shells*, in Proceedings of the IUTAM Symposium on the Theory of Thin Elastic Shells (Delft, 1959), North–Holland, Amsterdam, 1960, pp. 12–33.

[32] W. T. Koiter, *On the foundations of the linear theory of thin elastic shells. I*, II, Nederl. Akad. Wetensch. Proc. Ser. B, 73 (1970), pp. 169–182.

[33] G. D. C. Kuiken, *Wave propagation in a thin-walled liquid-filled initially stressed tube*, J. Fluid Mech., 141 (1984), pp. 289–308.

[34] P. Luchini, M. Lupo, and A. Pozzi, *Unsteady Stokes flow in a distensible pipe*, Z. Angew. Math. Mech., 71 (1991), pp. 367–378.

[35] X. Ma, G. C. Lee, and S. G. Lu, *Numerical simulation for the Propagation of nonlinear pulsatile waves in arteries*, ASME J. Biomech. Eng., 114 (1992), pp. 490–496.

[36] E. Marušić-Paloka and A. Mikelić, *The derivation of a nonlinear filtration law including the inertia effects via homogenization*, Nonlinear Anal., 42 (2000), pp. 97–137.

[37] A. Mikelić, *Homogenization theory and applications to filtration through porous media*, in Filtration in Porous Media and Industrial Applications, Lecture Notes in Math. 1734, M. Espedal, A. Fasano, and A. Mikelić, eds., Springer, Berlin, 2000, pp. 127–214.

[38] A. Mikelić, G. Guidoboni, and S. Čanić, *Fluid-Structure Interaction between a Vis-*

cous Incompressible Fluid and a Linearly Elastic Cylinder with Finite Wall Thickness, manuscript.

[39] W. W. Nichols and M. F. O'Rourke, *McDonald's Blood Flow in Arteries: Theoretical, Experimental and Clinical Principles*, 4th ed., Arnold, Oxford University Press, New York, London, Sydney, Auckland, 1997.

[40] F. Nobile, *Numerical Approximation of Fluid-Structure Interaction Problems with Application to Haemodynamics*, Ph.D. thesis, EPFL, Lausanne, Switzerland, 2001.

[41] V. Novozhilov, *Thin Shell Theory*, P. G. Lowe, ed., Groningen, Noordholf, The Netherlands 1964.

[42] M. S. Olufsen, C. S. Peskin, W. Y. Kim, E. M. Pedersen, A. Nadim, and J. Larsen, *Numerical simulation and experimental validation of blood flow in arteries with structured-tree outflow conditions*, Ann. Biomed. Eng., 28 (2000), pp. 1281–1299.

[43] G. Pontrelli, *A mathematical model of flow in a liquid-filled visco-elastic tube*, Med. Biol. Eng. Comput., 40 (2002), pp. 550–556.

[44] A. Quarteroni, M. Tuveri, and A. Veneziani, *Computational vascular fluid dynamics: Problems, models and methods. Survey article*, Comput. Vis. Sci., 2 (2000), pp. 163–197.

[45] H. Reismann, *Elastic Plates: Theory and Applications*, Wiley, New York, 1988.

[46] A. M. Robertson and A Sequeira, *A director theory approach to modeling blood flow in the arterial system: An alternative to classical* 1D *models*, Math. Models Methods Appl. Sci., 15 (2005), pp. 871–906.

[47] J. Tambača, S. Čanić, and A. Mikelić, *Effective model of the fluid flow through elastic tube with variable radius*, in XI. Mathematikertreffen Zagreb-Graz, Grazer Math. Ber. 348, Karl-Franzens-University, Graz, Austria, 2005, pp. 91–112.

[48] R. Temam, *Navier-Stokes Equations*, North–Holland, Amsterdam, 1984.

[49] H. B. da Veiga, *On the existence of strong solution to a coupled fluid structure evolution problem*, J. Math. Fluid Mech., 6 (2004), pp. 21–52.

[50] E. Ventsel and T. Krauthammer, *Thin Plates and Shells*, Marcel Dekker, New York, 2001.

[51] R. P. Vito and S. A. Dixon, *Blood vessels constitutive models* 1995-2002, Ann. Rev. Biomed. Eng., 5 (2003), pp. 413–439.

[52] A. Wempner, *Mechanics of Solids and Shells: Theories and Approximations*, CRC Press, Boca Raton, FL, 2003.